ELSEVIER
Journal of Contaminant Hydrology 16 (1994) 131–156
JOURNAL OF Contaminant Hydrology

A three-dimensional multiphase flow model for assessing NAPL contamination in porous and fractured media, 2. Porous medium simulation examples

S. Panday[a], Y.S. Wu[a], P.S. Huyakorn[a], E.P. Springer[b]
[a]*HydroGeoLogic, Inc., Suite 900, 1165 Herndon Parkway, Herndon, VA 22070, USA*
[b]*EES-15, Los Alamos National Laboratory, Los Alamos, NM 87545, USA*

(Received July 14, 1993; revision accepted March 1, 1994)

Abstract

This paper discusses the verification and application of the three-dimensional (3-D) multiphase flow model presented by Huyakorn et al. (Part 1 in this issue) for assessing contamination due to subsurface releases of non-aqueous-phase liquids (NAPL's). Attention is focussed on situations involving one-, two- and three-dimensional flow through porous media. The model formulations and numerical schemes are tested for highly nonlinear field conditions. The utility and accuracy of various simplifications to certain simulation scenarios are assessed. Five simulation examples are included for demonstrative purposes. The first example verifies the model for vertical flow and compares the performance of the fully three-phase and the passive-air-phase formulations. Air-phase boundary conditions are noted to have considerable effects on simulation results. The second example verifies the model for cross-sectional analyses involving LNAPL and DNAPL migration. Finite-difference (5-point) and finite-element (9-point) spatial approximations are compared for different grid aspect ratios. Unless corrected, negative-transmissivity conditions were found to have undesirable impact on the finite-element solutions. The third example provides a model validation against laboratory experimental data on 5-spot water-flood treatment of oil reservoirs. The sensitivity to grid orientation is noted for the finite-difference schemes. The fourth example demonstrates model utility in characterizing the 3-D migration of LNAPL and DNAPL from surface sources. The final example presents a modeling study of air sparging. Critical parameters affecting the performance of air-sparging system are examined. In general, the modeling results indicate sparging is more effective in water-retentive soils, and larger values of sparge influence radius may be achieved for certain anisotropic conditions.

SSDI 0169-7722(94)00013-8

1. Introduction

Modeling the behavior and subsurface migration of non-aqueous-phase (NAPL) contaminants requires an appropriate representation of the significant physical mechanisms, efficient and robust numerical solution schemes, and an understanding of the various simplifying assumptions that may be made for many practical situations. The first part of this study (Huyakorn et al., 1994 in this issue) presents mathematical formulations of the multiphase flow problem, and the numerical solution techniques necessary for practical field simulations. Various simplifications to the flow problem (e.g., the passive-air-phase formulation for a three-phase system, or the passive-liquid-phase formulation for air-sparging or vapor-extraction processes) have been discussed. Several options for spatial approximation, including 7-point finite-difference, 27-point finite-element, and 11-point (hybrid) three-dimensional (3-D) lattices, as well as their two-dimensional (2-D) counterparts, have been implemented in the model. The aim of this paper is to verify the model and its numerical schemes, present benchmark problems for code verification, examine the validity of the various simplifying assumptions, demonstrate the accuracy of the numerical schemes, and discuss applicability of the model to various field situations.

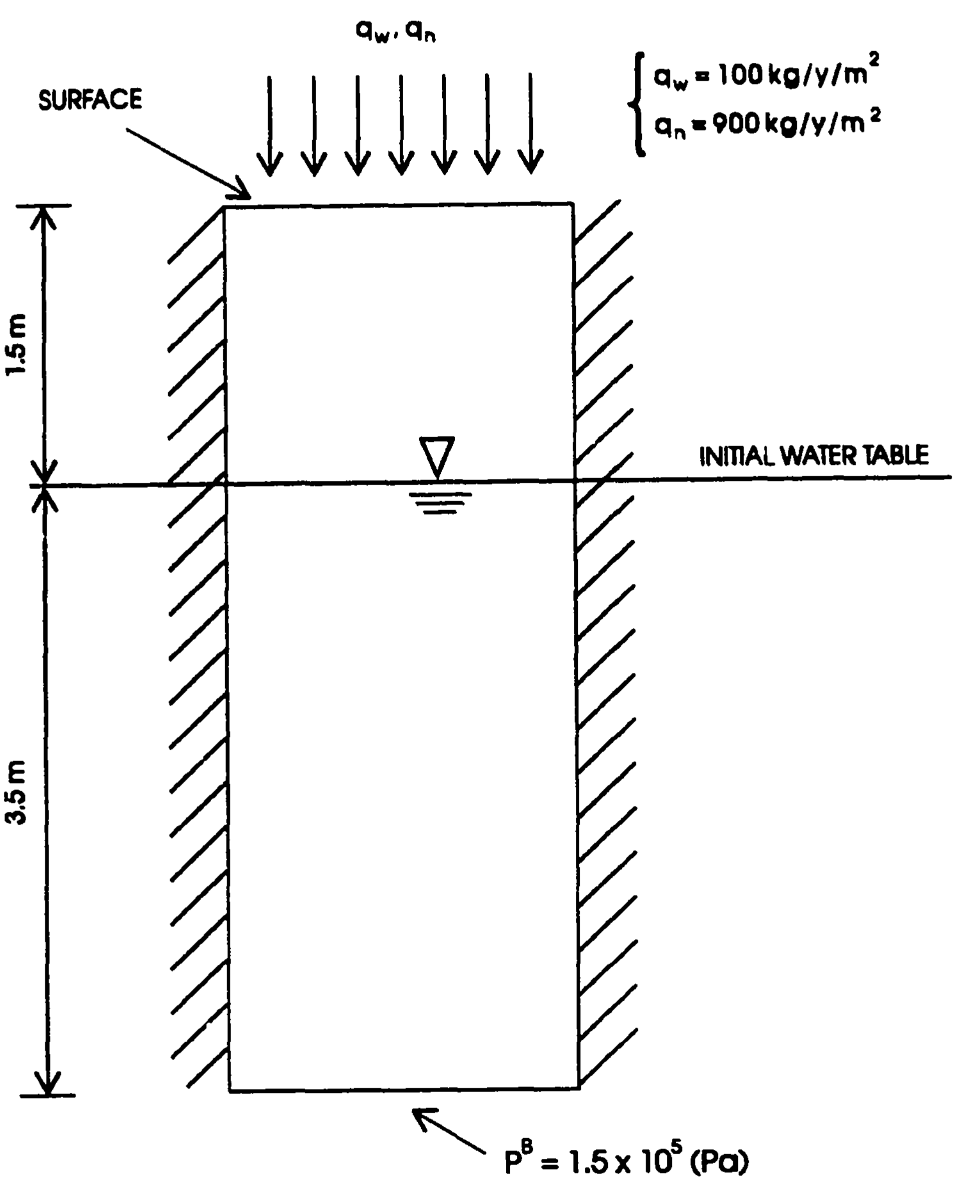

Fig. 1. Geometry and boundary conditions for simulation of vertical NAPL infiltration in a soil column.

A survey of documented numerical models and modeling efforts for subsurface NAPL contamination indicates few publications detailing how the various simplifying assumptions and numerical techniques affect the simulation results. This is because most, if not all of the previous models do not incorporate a flexibility in formulation, which allows the use of not only the most general three-phase flow equations but also their reduced forms, for special cases where the simplifying assumptions are justified. Presently, there is still a lack of assessment as to how well the passive air-phase formulation performs in depicting the three-phase flow behavior and saturation distributions; notwithstanding the passive air assumption being unjustifiable if the air-phase dynamics are important. There is also a need to study the performances of the various spatial approximation schemes as applied to field problems. For example, the sensitivity of grid orientation effects to various spatial approximations have not been examined even for the typical 5-spot well flow scenarios, commonly described in the petroleum literature (Yasonik and McCracken, 1979; Thomas, 1982; Willhite, 1986). The impact of negative transmissibilities for certain grid aspect ratios in finite-element models also needs to be studied for the multiphase flow case. A grid aspect ratio of $\sqrt{2}:1$ (Forsyth, 1988) can lead to unacceptable negative-transmissibility conditions for an isotropic rectangular prism element, severely hindering convergence and producing physically incorrect results. Practical 3-D field simulations will become prohibitive if severe gridding restrictions are imposed to avoid negative transmissibilities. The current study examines these effects to provide a better understanding of the accuracy and reliability of the various popular numerical schemes used.

Five simulation examples are included in this paper. The first example serves to verify the code and its solution schemes against previously published results. The passive-air-phase formulation is compared with the fully three-phase formulation.

Table 1
Parameter values used in the simulation of vertical NAPL infiltration in a variably saturated soil column

Parameter	Value
Permeability, k	$1 \cdot 10^{-12}$ m^2
Porosity, ϕ	0.3
Cross-sectional area, A	1.0 m^2
Column length, L	5.0 m
Depth to water table, H	1.5 m
Atmospheric pressure, P_{atm}	10^5 Pa (N m^{-2})
Initial water density, ρ_w^o	1,000 kg m^{-3}
Initial NAPL density, ρ_n^o	950 kg m^{-3}
Water viscosity, μ_w	$1 \cdot 10^{-3}$ Pa s
NAPL viscosity, μ_n	$1 \cdot 10^{-3}$ Pa s
Water compressibility, β_w	$4.3 \cdot 10^{-9}$ Pa^{-1}
NAPL compressibility, β_n	$3.0 \cdot 10^{-9}$ Pa^{-1}
Porous medium compressibility, β_s	10^{-10} Pa^{-1}
Water injection rate, q_w	100 kg yr^{-1} m^{-2}
NAPL injection rate, q_n	900 kg yr^{-1} m^{-2}
Bottom pressure, $p^B = p_w^B = (p_n^B$	$1.5 \cdot 10^5$ Pa

Table 2
Relative permeability and capillary pressure data used in the simulation of vertical NAPL infiltration in a variably saturated soil column

Two-phase water–NAPL (wn) system

S_w	k_{rw}	k_{rn}^{wn}	P_{cnw} (Pa)
0.2	0.00	0.68	$0.90 \cdot 10^4$
0.3	0.04	0.55	$0.54 \cdot 10^4$
0.4	0.10	0.43	$0.39 \cdot 10^4$
0.5	0.18	0.31	$0.33 \cdot 10^4$
0.6	0.30	0.20	$0.30 \cdot 10^4$
0.7	0.44	0.12	$0.27 \cdot 10^4$
0.8	0.60	0.05	$0.24 \cdot 10^4$
0.9	0.80	0.00	$0.15 \cdot 10^4$
1.0	1.00	0.00	0.0

Two-phase NAPL–air (na) and air–water (aw) systems

S_a	k_{ra}	k_{rn}^{na}	P_{can} (Pa)	P_{caw} (Pa)
0.00	0.00	0.680	0.00	0.00
0.10	0.01	0.490	$0.90 \cdot 10^3$	$0.10 \cdot 10^4$
0.20	0.04	0.340	$0.12 \cdot 10^4$	$0.20 \cdot 10^4$
0.30	0.09	0.210	$0.15 \cdot 10^4$	$0.30 \cdot 10^4$
0.40	0.16	0.116	$0.18 \cdot 10^4$	$0.33 \cdot 10^4$
0.50	0.25	0.045	$0.21 \cdot 10^4$	$0.36 \cdot 10^4$
0.60	0.36	0.009	$0.24 \cdot 10^4$	$0.39 \cdot 10^4$
0.68	0.46	0.000	$0.30 \cdot 10^4$	$0.45 \cdot 10^4$
0.80	0.64	0.000	$0.90 \cdot 10^4$	$0.66 \cdot 10^4$

The effects of air-phase surface boundary conditions on the simulation results are demonstrated. The second example also serves to test code performance for cross-sectional analyses of the subsurface migration of light NAPL's (LNAPL's) and dense NAPL's (DNAPL's). This example demonstrates a case where both the 5-point (finite-difference) and 9-point (finite-element) lattices for 2-D perform fairly well. It further depicts an instance where the conventional 9-point finite-element approximation produces negative-transmissibility conditions leading to unacceptable convergence behavior. The third example tests the performances of finite-difference and finite-element lattices on 2-D (areal) simulations with different grid orientations and aspect ratios. The fourth example demonstrates application of the model to 3-D field scenarios involving LNAPL and DNAPL plumes emanating from surface sources. The fifth example provides a conceptual study of the air-sparging process. The passive-liquid-phase assumption is tested by comparing its resulting formulation with the rigorous two-phase formulation. The axi-symmetric option for modeling well flow is also verified using this example. Finally, various physical parameters that affect the air-sparging process are examined.

Table 3
Initial conditions used in the simulation of vertical NAPL infiltration in a variably saturated soil column

Depth (m)	P_n (N m^{-2} or Pa)	S_n	S_w
0.125	$0.9850 \cdot 10^5$	0.0	0.8500
0.375	$0.9877 \cdot 10^5$	0.0	0.8773
0.625	$0.9905 \cdot 10^5$	0.0	0.9045
0.875	$0.9932 \cdot 10^5$	0.0	0.9318
1.125	$0.9959 \cdot 10^5$	0.0	0.9591
1.375	$0.9986 \cdot 10^5$	0.0	0.9864
1.625	$0.1012 \cdot 10^6$	0.0	$0.1000 \cdot 10^1$
1.875	$0.1037 \cdot 10^6$	0.0	$0.1000 \cdot 10^1$
2.125	$0.1061 \cdot 10^6$	0.0	$0.1000 \cdot 10^1$
2.375	$0.1086 \cdot 10^6$	0.0	$0.1000 \cdot 10^1$
2.625	$0.1110 \cdot 10^6$	0.0	$0.1000 \cdot 10^1$
2.875	$0.1135 \cdot 10^6$	0.0	$0.1000 \cdot 10^1$
3.125	$0.1159 \cdot 10^6$	0.0	$0.1000 \cdot 10^1$
3.375	$0.1184 \cdot 10^6$	0.0	$0.1000 \cdot 10^1$
3.625	$0.1208 \cdot 10^6$	0.0	$0.1000 \cdot 10^1$
3.875	$0.1233 \cdot 10^6$	0.0	$0.1000 \cdot 10^1$
4.125	$0.1257 \cdot 10^6$	0.0	$0.1000 \cdot 10^1$
4.375	$0.1282 \cdot 10^6$	0.0	$0.1000 \cdot 10^1$
4.625	$0.1306 \cdot 10^6$	0.0	$0.1000 \cdot 10^1$
4.875	$0.1331 \cdot 10^6$	0.0	$0.1000 \cdot 10^1$

2. NAPL infiltration in a soil column

This problem was used to test the fully three-phase and the passive-air-phase (two-phase, water–NAPL, flow in a three-phase system) modeling options. A vertical, 5-m soil column (Fig. 1), with an initial water table 1.5 m below the surface, was injected with 900 kg yr^{-1} m^{-2} of NAPL and 100 kg yr^{-1} m^{-2} of water at the top. Water, NAPL and soil properties used for the simulation are shown in Table 1, and the relative permeability and capillary pressure data are shown in Table 2. These constitutive relations have been taken from the tabulated values given by Faust (1985) and Forsyth (1991). The initial conditions, shown in Table 3 represent a NAPL-free system. The bottom boundary was assigned pressure conditions of $p_W^B = p_n^B = 1.5 \cdot 10^5$ Pa for both water and NAPL. This represents a water-saturated condition ($S_w = 1$) till the NAPL front reaches this boundary.

The domain was discretized in three dimensions using a rectangular grid consisting of 20 brick elements and 84 nodes. A uniform nodal spacing of 0.25 m was used in the vertical direction. The simulation was first performed using the passive-air-phase formulation, and results were compared with numerical solutions from the NAPL3D model of Forsyth (1991), and the SAMFT1D model (Huyakorn et al., 1991). Water and NAPL saturation profiles at various times are shown in Figs. 2 and 3, respectively. The agreement between the results of the three models is excellent.

The same flow problem was reanalyzed using the fully three-phase formulation,

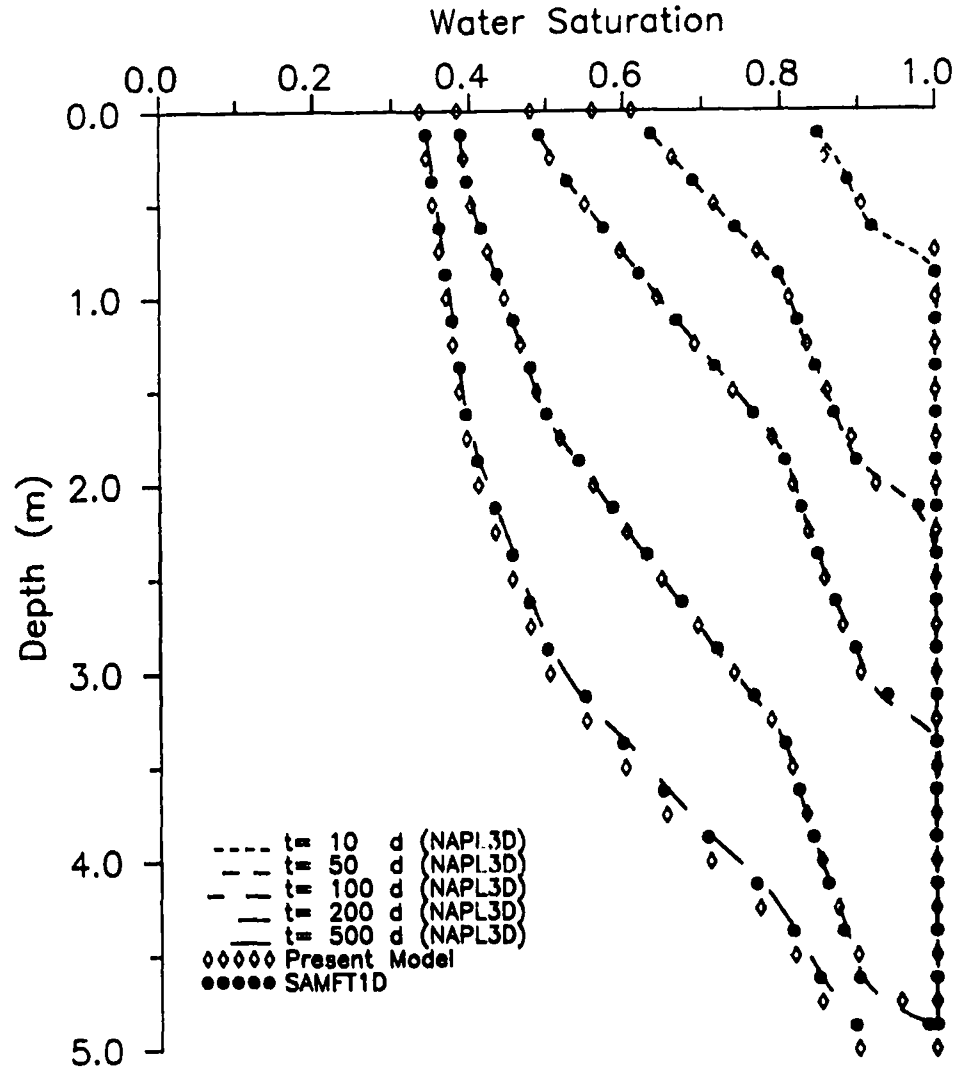

Fig. 2. Predicted water saturations for simulation of vertical NAPL infiltration in a variably saturated soil column using the passive-air-phase approach.

with initial atmospheric conditions, and a no-flow boundary condition for air at the top of the soil column. The impervious air boundary was selected to ease boundary condition implementation in all codes used in the comparative study. The current model was compared with SAMFT1D (Huyakorn et al., 1991) and a three-phase compositional code described by Forsyth and Shao (1991). The latter was chosen because the NAPL3D code mentioned earlier does not have the fully three-phase modeling option. Water and NAPL saturation profiles predicted at various times by the three models are shown in Figs. 4 and 5, respectively. All three numerical solutions are generally in good agreement, with slight differences near the surface. Note that the compositional model requires water to exist as a component in the air phase, thus creating the deviation from the other two models. We further assess the behavior of numerical solutions by cross-checking Figs. 4 and 5 with Figs. 2 and 3. These comparisons indicate that the passive-air-phase formulation produce similar saturation profiles to the fully three-phase simulation. Near the surface of the soil column, however, the results are considerably different, primarily due to the impermeable boundary condition for the air-flow equation in the second simulation, which causes the displaced air to accumulate beneath the surface. Note that a fully three-phase simulation with atmospheric pressure Dirichlet boundary condition at the top gives saturation profiles almost identical to Figs. 2 and 3, since the displaced air escapes through the surface.

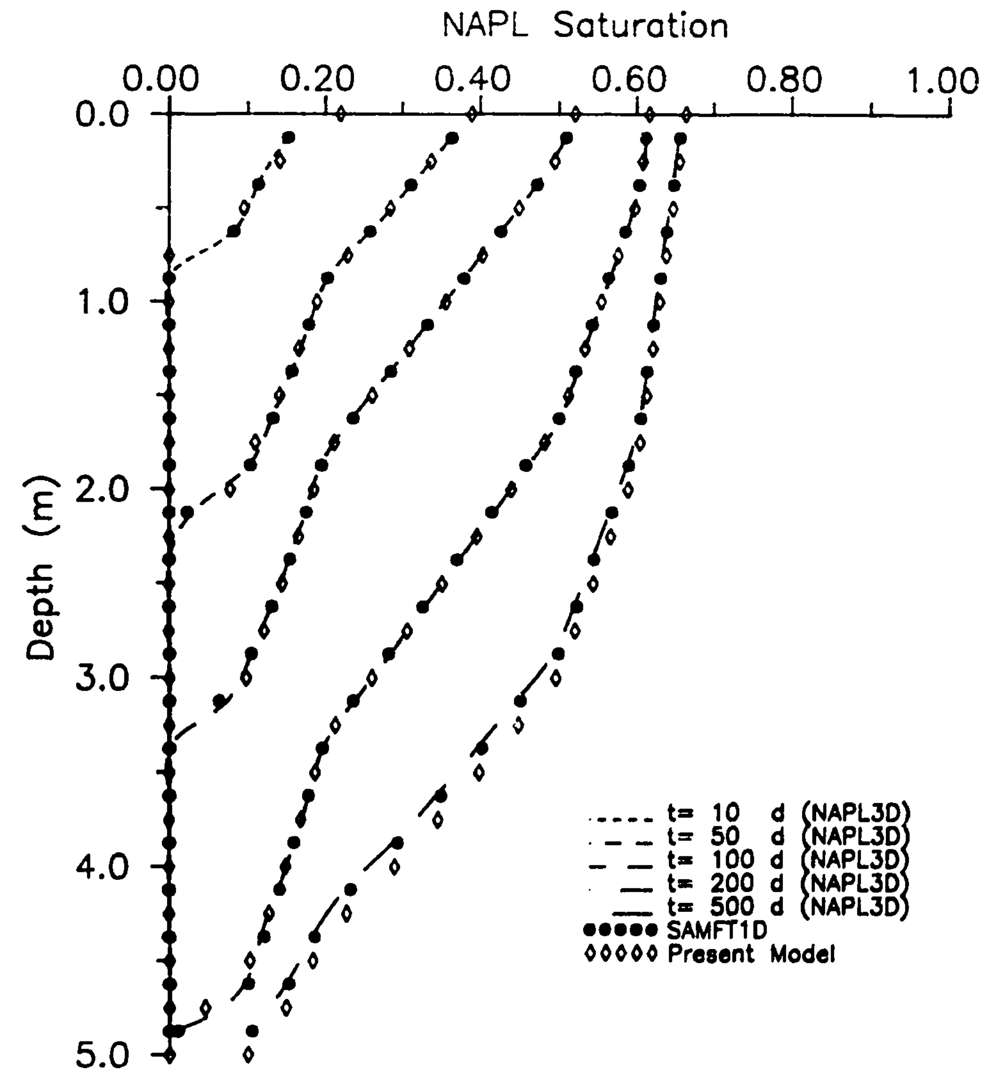

Fig. 3. Predicted NAPL saturations for simulation of vertical NAPL infiltration in a variably saturated soil column using the passive-air-phase approach.

3. Cross-sectional analysis of LNAPL and DNAPL migration in vadose zone and unconfined aquifer

This problem corresponds to the cross-sectional problem of Faust (1985), and was selected to verify the model for 2-D migration of NAPL from a continuous source at the soil surface. The simulation domain (Fig. 6) represents a surficial unit 5 m thick and 16.9 m in length. The system is subject to water infiltration at a rate of 0.1 m yr^{-1} (100 kg yr^{-1} m^{-2}). The NAPL source with a release rate of 900 kg yr^{-1} is located at the top left edge. The surficial unit has a shallow water table (1.5 m deep) and is underlain by a draining aquifer. The left- and right-hand boundaries of the domain were treated as impermeable, and the bottom boundary was assigned constant-pressure conditions with $p_n^B = 1.3185 \cdot 10^5$ Pa and $p_W^B = 1.2495 \cdot 10^5$ Pa. The value of p_W^B was calculated from two-phase NAPL–water capillary data assuming $S_w = 1$ at the bottom boundary, adjacent to the draining aquifer. Values of physical parameters used in the simulation are depicted in Table 4. Initial conditions and tabulated constitutive relations are presented in Tables 5 and 6, respectively. Absolute pressure values depicted in Table 5 were derived from Faust's (1985) gauge pressure values. To be consistent with his modeling assumptions, the air–water capillary pressure, p_{caw}, was further evaluated as $p_{caw} = p_{can} + p_{cnw}$ even in zones where NAPL was absent. Strictly speaking, p_{caw} should be determined independently from p_{can} and p_{cnw} using

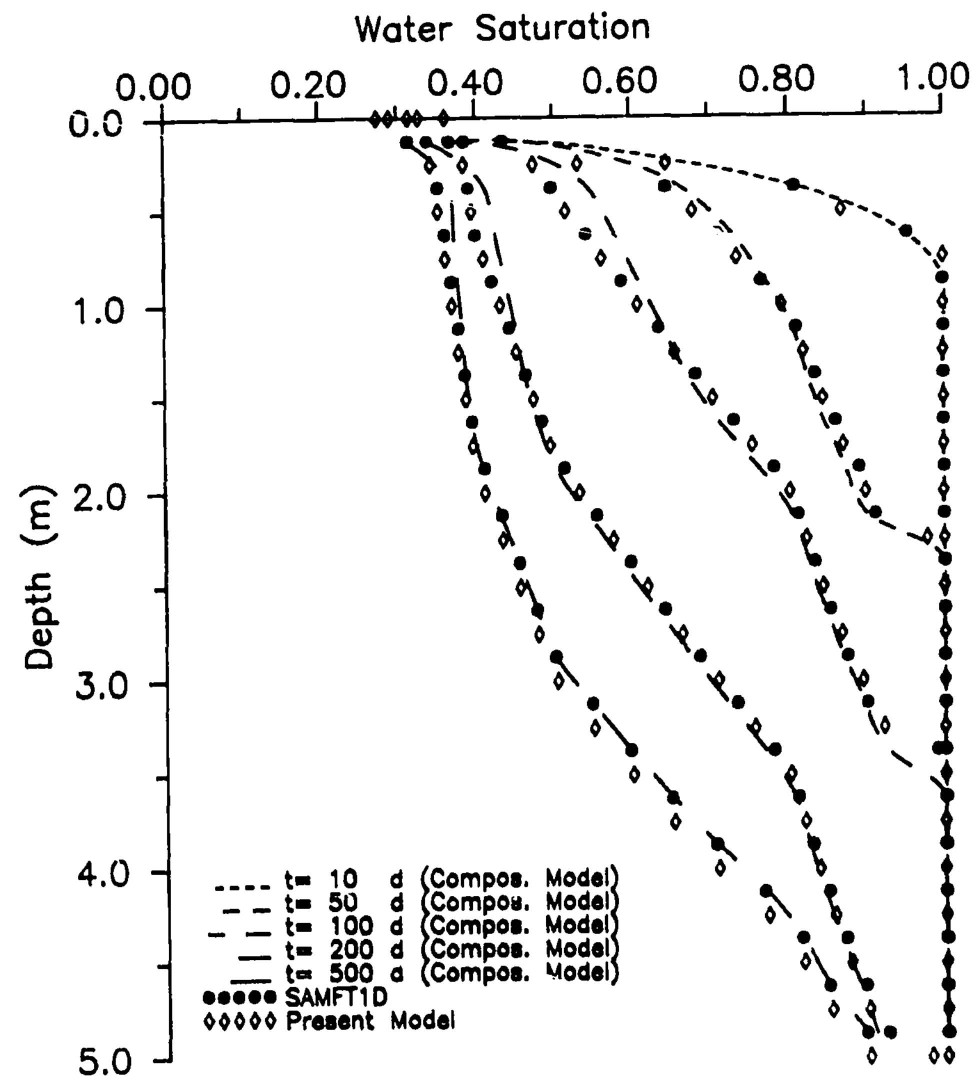

Fig. 4. Predicted water saturations for simulation of vertical NAPL infiltration in a variably saturated soil column using the fully three-phase approach.

data for the two-phase, air–water system to correctly represent the state of the pristine portions of the domain.

The domain was discretized using a 2-D rectangular grid consisting of 120 (6 × 20) elements and 147 nodes. Nodal spacings along the horizontal axis were 1, 1.41, 2, 2.83, 4 and 5.66 m, respectively. A uniform nodal spacing of 0.25 m was used along the vertical axis. An initial time-step of 10,000 s was used. Subsequent time-step values were calculated using the aggressive variable time-stepping algorithm, described in Part 1, with a maximum Δt_{max} of 864,000 s (10 days). Two cases involving a DNAPL ($\rho_n = 1200$ kg m^{-3}) and an LNAPL ($\rho_n = 950$ kg m^{-3}) were solved using the passive-air-phase formulation with the finite-difference (5-point) lattice option. The simulated saturation contours are shown in Figs. 6 and 7 for the DNAPL and LNAPL cases, respectively. The DNAPL sinks below the water table and drains through the base, while LNAPL is seen to spread horizontally and float on the water table. For both situations, the saturation distributions predicted by the present model are in good agreement with Faust's (1985) results. The LNAPL case was reanalyzed using the 9-point finite-element lattice option. The resulting LNAPL saturation distribution is also plotted in Fig. 7 and seen to be in excellent agreement with the corresponding numerical solution obtained using the 5-point, finite-difference stencil. No numerical difficulty was encountered with the finite-element approximation scheme used in our model because negative-transmissivity

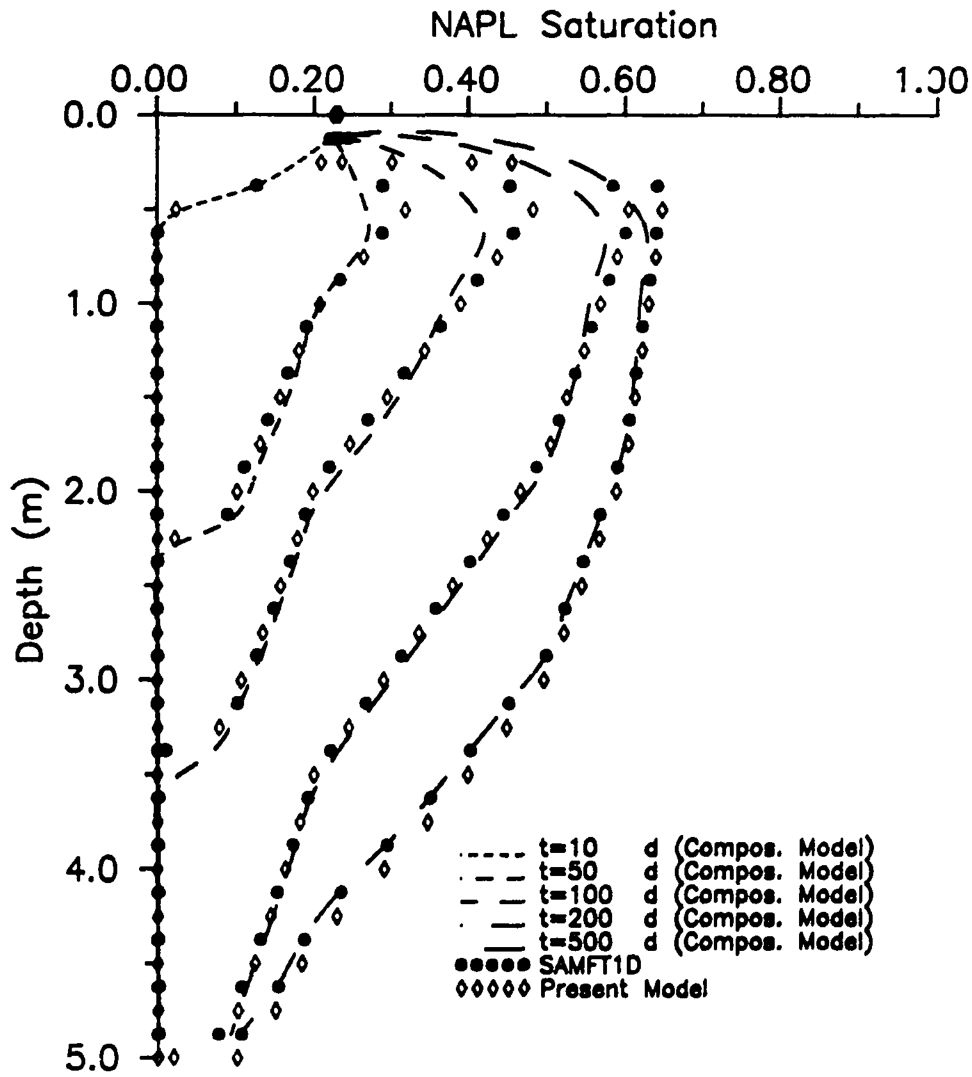

Fig. 5. Predicted NAPL saturations for simulation of vertical NAPL infiltration in a variably saturated soil column using the fully three-phase approach.

conditions were alleviated as discussed in Part 1 (Huyakorn et al., this issue). However, convergence was hindered with the 9-point finite-element approximation, when the conventional Galerkin or weighted residual formulations were used, even with full upstream weighting. This is due to the occurrence of negative transmissibilities, which also resulted in oscillatory, negative-saturation profiles. This simulation was finally aborted after $t = 100$ days since the time-step size was reduced below 60 s, the minimum allowable step size.

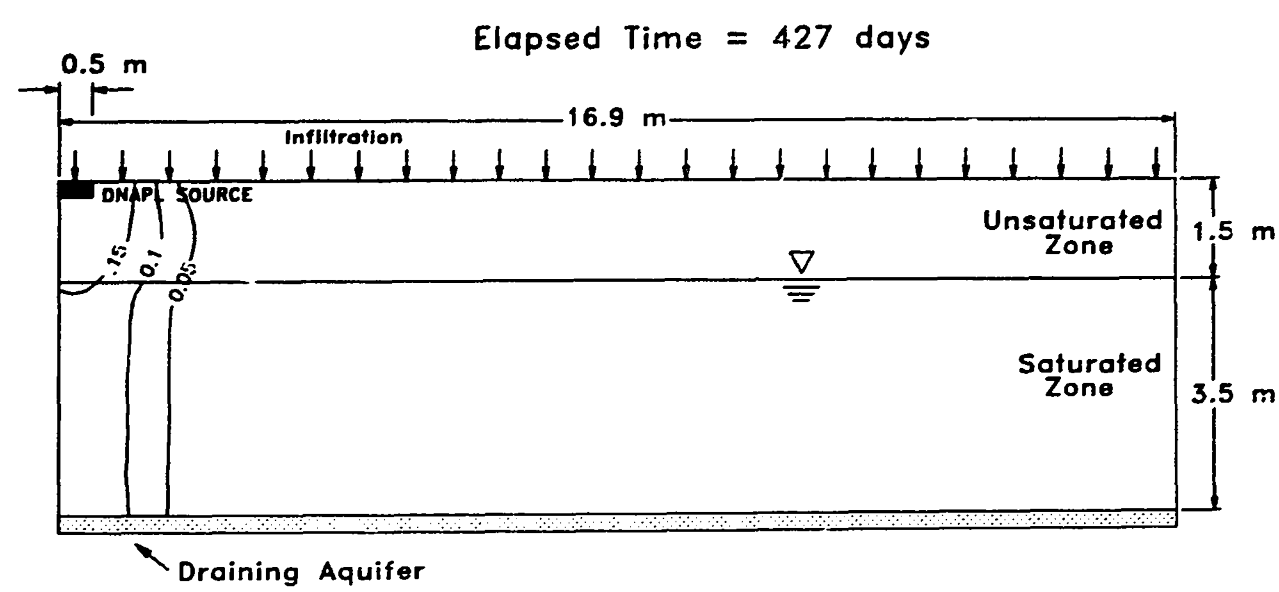

Fig. 6. DNAPL saturation profile for cross-sectional simulation of NAPL migration in a surficial aquifer.

Table 4
Physical parameter values used in the cross-sectional analysis of migration of LNAPL and DNAPL in a draining aquifer

Parameter	Value
Permeability, k	$1\cdot10^{-12}$ m^2
Porosity, Θ	0.3
Water density, ρ_w	1,000 kg m^{-3}
Water viscosity, μ_w	$1\cdot10^{-3}$ Pa s
Density, ρ_n, LNAPL (case *1*)	950 kg m^{-3}
Density, ρ_n, DNAPL (case *2*)	1,200 kg m^{-3}
Viscosity, μ_n, LNAPL and DNAPL	$1\cdot10^{-3}$ Pa s
Water injection infiltration rate, q_w	100 kg yr^{-1} m^{-2}
Total NAPL injection rate, Q_n	900 kg yr^{-1}
Bottom water pressure, P_w	$1.2495\cdot10^5$ Pa
Bottom NAPL pressure, P_n	$1.3185\cdot10^5$ Pa

Table 5
Initial conditions used in the cross-sectional analysis of LNAPL and DNAPL migration in a draining aquifer

Depth (m)	P_n (N m^{-2} or Pa)	S_n	S_w
0.125	$0.761237\cdot10^5$	0.0	0.8500
0.375	$0.783879\cdot10^5$	0.0	0.8700
0.625	$0.817841\cdot10^5$	0.0	0.9000
0.875	$0.846143\cdot10^5$	0.0	0.9250
1.125	$0.874446\cdot10^5$	0.0	0.9500
1.375	$0.902748\cdot10^5$	0.0	0.9750
1.625	$0.943308\cdot10^5$	0.0	$0.1000\cdot10^1$
1.875	$0.967825\cdot10^5$	0.0	$0.1000\cdot10^1$
2.125	$0.992341\cdot10^5$	0.0	$0.1000\cdot10^1$
2.375	$0.101686\cdot10^6$	0.0	$0.1000\cdot10^1$
2.625	$0.104137\cdot10^6$	0.0	$0.1000\cdot10^1$
2.875	$0.106589\cdot10^6$	0.0	$0.1000\cdot10^1$
3.125	$0.109041\cdot10^6$	0.0	$0.1000\cdot10^1$
3.375	$0.111492\cdot10^6$	0.0	$0.1000\cdot10^1$
3.625	$0.113944\cdot10^6$	0.0	$0.1000\cdot10^1$
3.875	$0.116396\cdot10^6$	0.0	$0.1000\cdot10^1$
4.125	$0.118847\cdot10^6$	0.0	$0.1000\cdot10^1$
4.375	$0.121299\cdot10^6$	0.0	$0.1000\cdot10^1$
4.625	$0.123751\cdot10^6$	0.0	$0.1000\cdot10^1$
4.875	$0.126202\cdot10^6$	0.0	$0.1000\cdot10^1$

Table 6
Relative permeability and capillary pressure date used in the cross-sectional analysis of LNAPL and DNAPL migration in a draining aquifer

Two-phase water–NAPL system

S_w	k_{rw}	k_{rn}^{wn}	P_{cnw} (Pa)
0.2000	0.0000	0.6800	$0.1034 \cdot 10^6$
0.3000	$0.4000 \cdot 10^{-1}$	0.5500	$0.2758 \cdot 10^5$
0.4000	0.1000	0.4300	$0.1034 \cdot 10^5$
0.5000	0.1800	0.3100	$0.7585 \cdot 10^4$
0.6000	0.3000	0.2000	$0.7447 \cdot 10^4$
0.7000	0.4400	0.1200	$0.7309 \cdot 10^4$
0.8000	0.6000	$0.5000 \cdot 10^{-1}$	$0.7171 \cdot 10^4$
0.9000	0.8000	0.0000	$0.7033 \cdot 10^4$
$0.1000 \cdot 10^1$	$0.1000 \cdot 10^1$	0.0000	$0.6895 \cdot 10^4$

Two-phase NAPL–air and air–water systems

S_a	k_{ra}	k_{rn}^{na}	P_{can} (Pa)	P_{caw} (Pa)
0.0000	0.0000	0.6800	0.0000	$0.6895 \cdot 10^4$
0.6800	0.6800	0.0000	$0.6664 \cdot 10^5$	$0.8388 \cdot 10^5$
0.8000	0.8000	0.0000	$0.7710 \cdot 10^5$	$0.1805 \cdot 10^6$

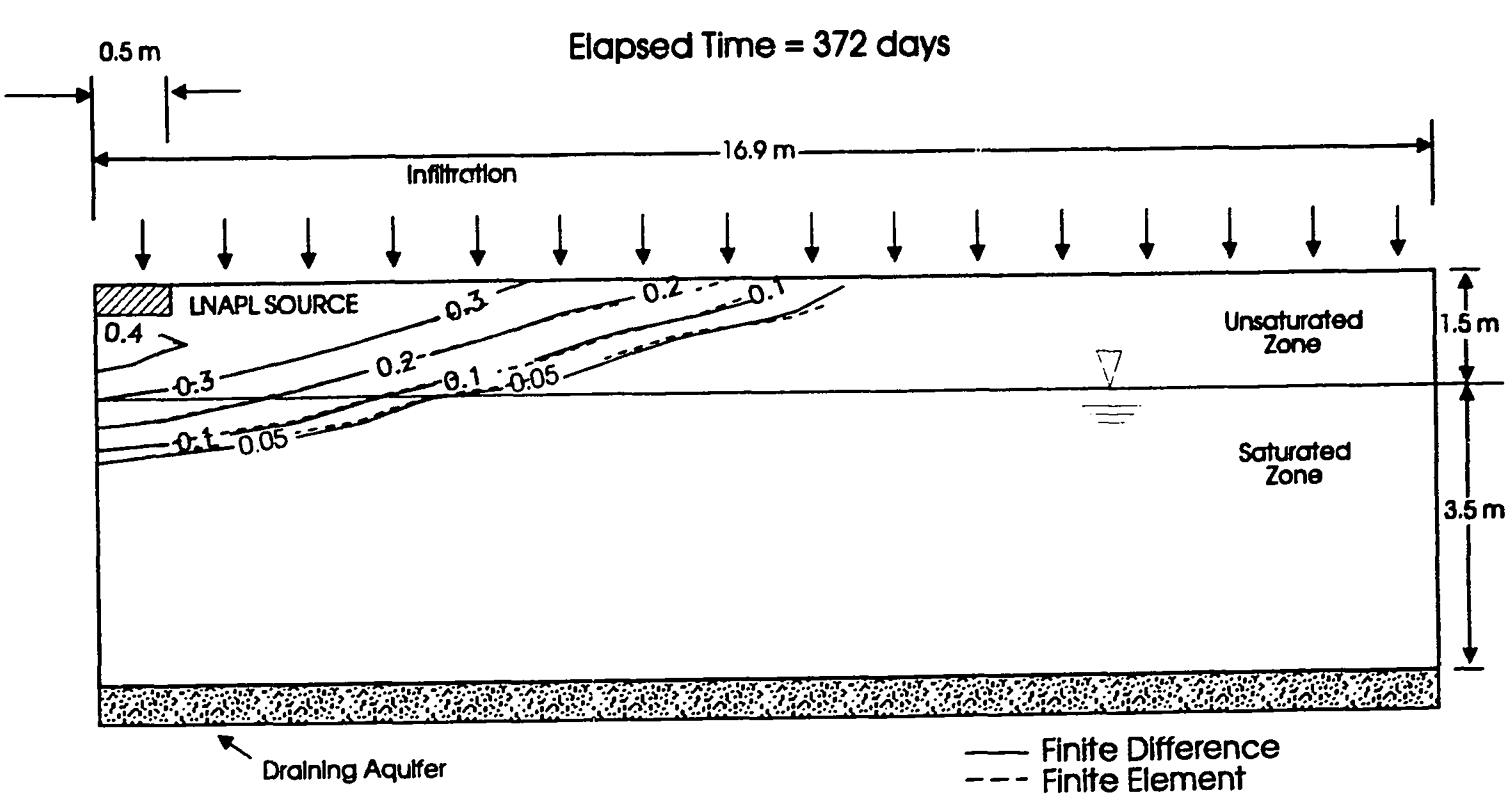

Fig. 7. Flow system and resulting LNAPL saturation contours for cross-sectional simulation of NAPL migration in a surficial aquifer.

4. 5-Spot water-flood analysis

This problem was selected to test the code with parallel and diagonal grids, using the finite-element and finite-difference nodal connectivities. The example corresponds to one of the laboratory 5-spot water floods described by Gaucher and Lindley (1960), and hence also serves to validate the model with scaled laboratory experiments. The 5-spot well pattern is depicted in Fig. 8. Water is injected into the recharging wells to displace the resident oil towards the withdrawal wells. This problem can be simulated using either a diagonal grid or parallel grid because of symmetry. Square grids (1:1 aspect ratio) were first selected to assess the behavior of numerical solution. The diagonal grid was comprised of 11 rows and 11 columns, while the parallel grid was made up of 15 rows and 15 columns; thus the nodal spacings of both grids were kept approximately the same for comparable accuracy. Each well node was assigned only one-quarter of the given well fluxes due to symmetric considerations. The material parameters used for the simulations are shown in Table 7.

The simulations were performed using the 5-point, finite-difference and the 9-point, finite-element lattice options. Fig. 9 shows a comparison of the simulated and experimental cumulative oil recovery curves. In general, both the model results are in good agreement with the experimental data. The saturation distributions at 14 yr, produced

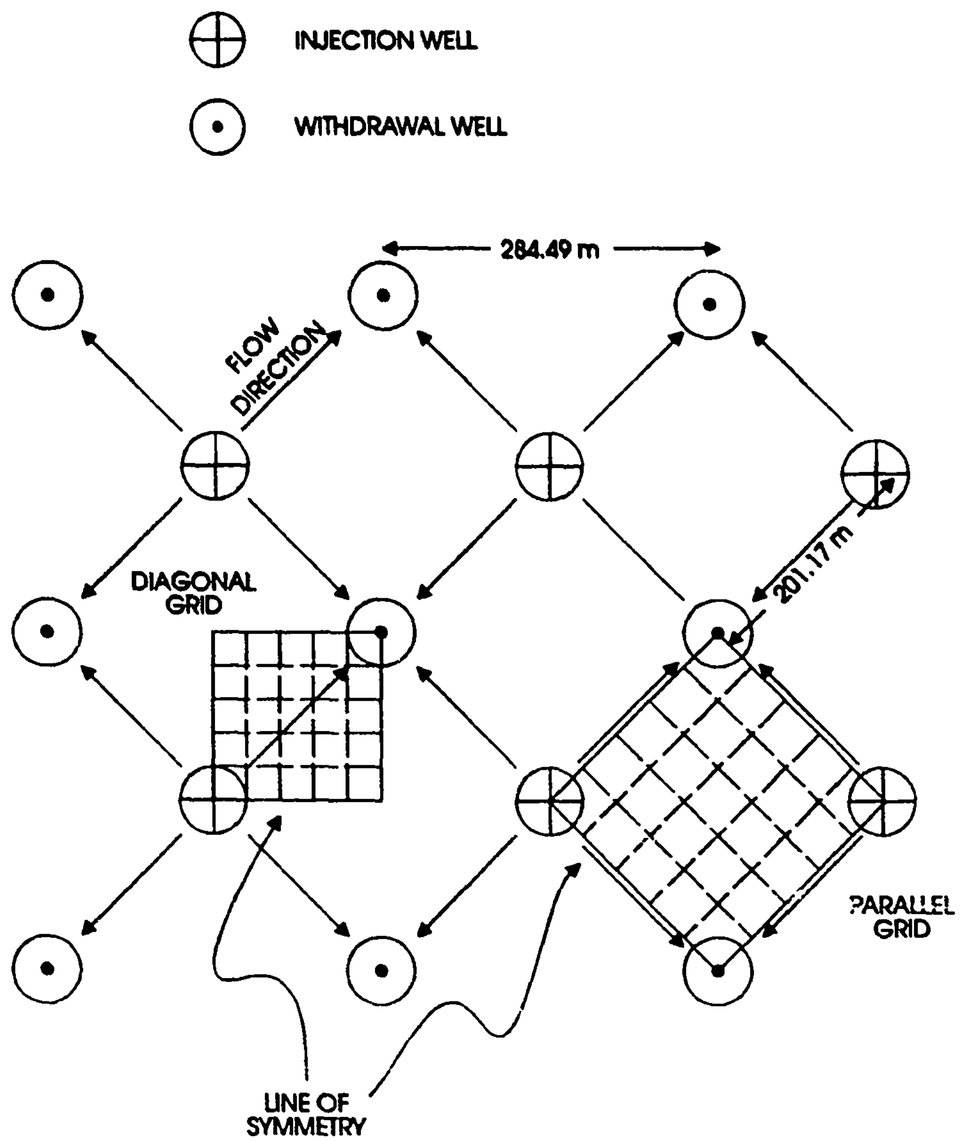

Fig. 8. Schematic of the 5-spot water-flood problem.

Table 7
Data used in the reservoir-scale simulation of a water flood 5-spot laboratory experiment reported by Gaucher and Lindley (1960)

Parameter	Value
Water injection rate, Q_w	$1.27472 \cdot 10^{-2}$ kg s^{-1} per well
Total liquid production rate, Q_L	$1.27472 \cdot 10^{-2}$ kg s^{-1} per well
Intrinsic permeability, k	$1.579 \cdot 10^{-12}$ m^2
Porosity, ϕ	0.2
Oil density, ρ_n	800 kg m^{-3}
Oil viscosity, μ_n	2.17 cP
Water density, ρ_w	1,000 kg m^{-3}
Water viscosity, μ_w	0.5 cP
Residual water saturation, S_{wr}	0.3
Residual oil saturation, S_{nr}	0.067
Water relative permeability at residual oil saturation, k_{rw}*	0.562
Oil relative permeability at residual water saturation, k_{rn}*	0.813
Initial oil saturation, $S_{n(t=0)}$	0.7

S_w	k_{rw}	k_{rn}	p_c (Pa)
0.30000	0.00000	0.81250	$0.4434 \cdot 10^5$
0.33164	0.00000	0.75002	$0.3810 \cdot 10^5$
0.36328	0.00000	0.68935	$0.3295 \cdot 10^5$
0.39492	0.00000	0.63055	$0.2863 \cdot 10^5$
0.42656	0.00000	0.57365	$0.2495 \cdot 10^5$
0.45820	0.00001	0.51870	$0.2177 \cdot 10^5$
0.48984	0.00005	0.46578	$0.1901 \cdot 10^5$
0.52148	0.00016	0.41492	$0.1658 \cdot 10^5$
0.55312	0.00046	0.36622	$0.1443 \cdot 10^5$
0.58476	0.00115	0.31973	$0.1251 \cdot 10^5$
0.61640	0.00261	0.27556	$0.1079 \cdot 10^5$
0.64804	0.00547	0.23379	$0.9237 \cdot 10^4$
0.67968	0.01073	0.19455	$0.7828 \cdot 10^4$
0.71132	0.01996	0.15797	$0.6545 \cdot 10^4$
0.74296	0.03545	0.12420	$0.5371 \cdot 10^4$
0.77460	0.06051	0.09346	$0.4293 \cdot 10^4$
0.80624	0.09979	0.06598	$0.3300 \cdot 10^4$
0.83788	0.15963	0.04212	$0.2381 \cdot 10^4$
0.86952	0.24860	0.02238	$0.1530 \cdot 10^4$
0.90116	0.37799	0.00759	$0.7380 \cdot 10^3$
0.93280	0.56250	0.00000	0.0000

by the diagonal and parallel grids, are compared in Figs. 10 and 11 for the finite-difference and finite-element schemes, respectively. As may be noted, the 9-point finite-element solution is less sensitive to grid orientation than its finite-difference counterpart. With the use of a parallel grid, the 5-point lattice tends to produce diamond-shaped, rather than rounded, saturation contours surrounding the injection wells.

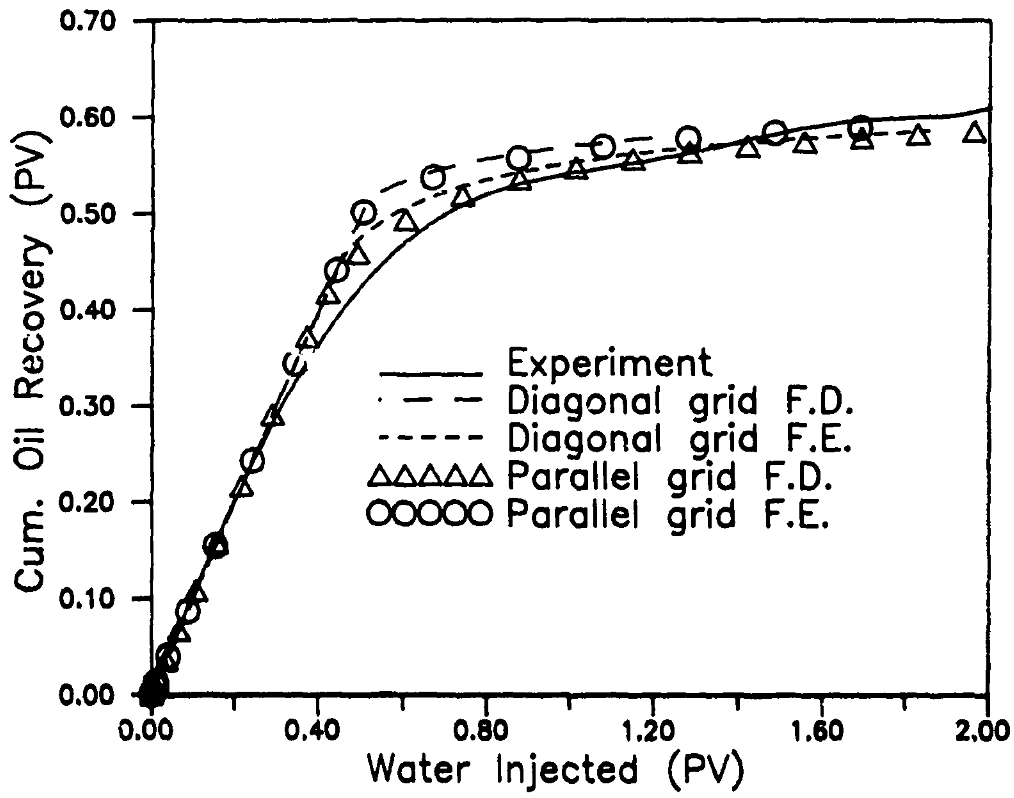

Fig. 9. A comparison of numerical and experimental cumulative oil recovery curves for the 5-spot waterflood problem.

As a further test of the accuracy and robustness of the 9-point finite-element modeling option, the same flow problems were solved using two additional, diagonal and parallel grids, with a 2:1 aspect ratio. A comparison of the resulting water saturation distributions at 14 yr is shown in Fig. 12. These numerical solutions are noted to be of similar accuracy to the previous finite-element results (Fig. 11) which were obtained from the square grids. The model performance was efficient for all cases. Typically, it took ~ 40 time steps to reach 14 yr, with a total of ~ 160 matrix solutions. For demonstrative purposes, the original upstream Galerkin formulation (without eliminating negative transmissivity terms) was also used to analyze the same problem. The simulations for both diagonal and parallel grids failed for this case at ~ 14 yr, after a total of ~ 60 time steps and 400 matrix iterations, due to convergence difficulties which led to a drastically reduced time-step size. Fig. 13 shows the water saturation contours for this simulation. The predicted saturation distributions are seen to be inaccurate, and indeed, spurious negative saturation values and oscillations were encountered.

5. 3-D simulation of NAPL contamination in a shallow aquifer

This example problem concerns the contamination of a shallow aquifer system due to two NAPL sources; source *1* releasing NAPL continuously at a rate of 1800 kg yr^{-1} and source *2* releasing NAPL at a rate of 900 kg yr^{-1} for a period of 100 days. The domain geometry and locations of the sources are depicted in Fig. 14. The immiscible contaminant, emanating from the sources, flows through ~ 1 m of the vadose zone into a groundwater system with an ambient hydraulic head gradient of 0.01.

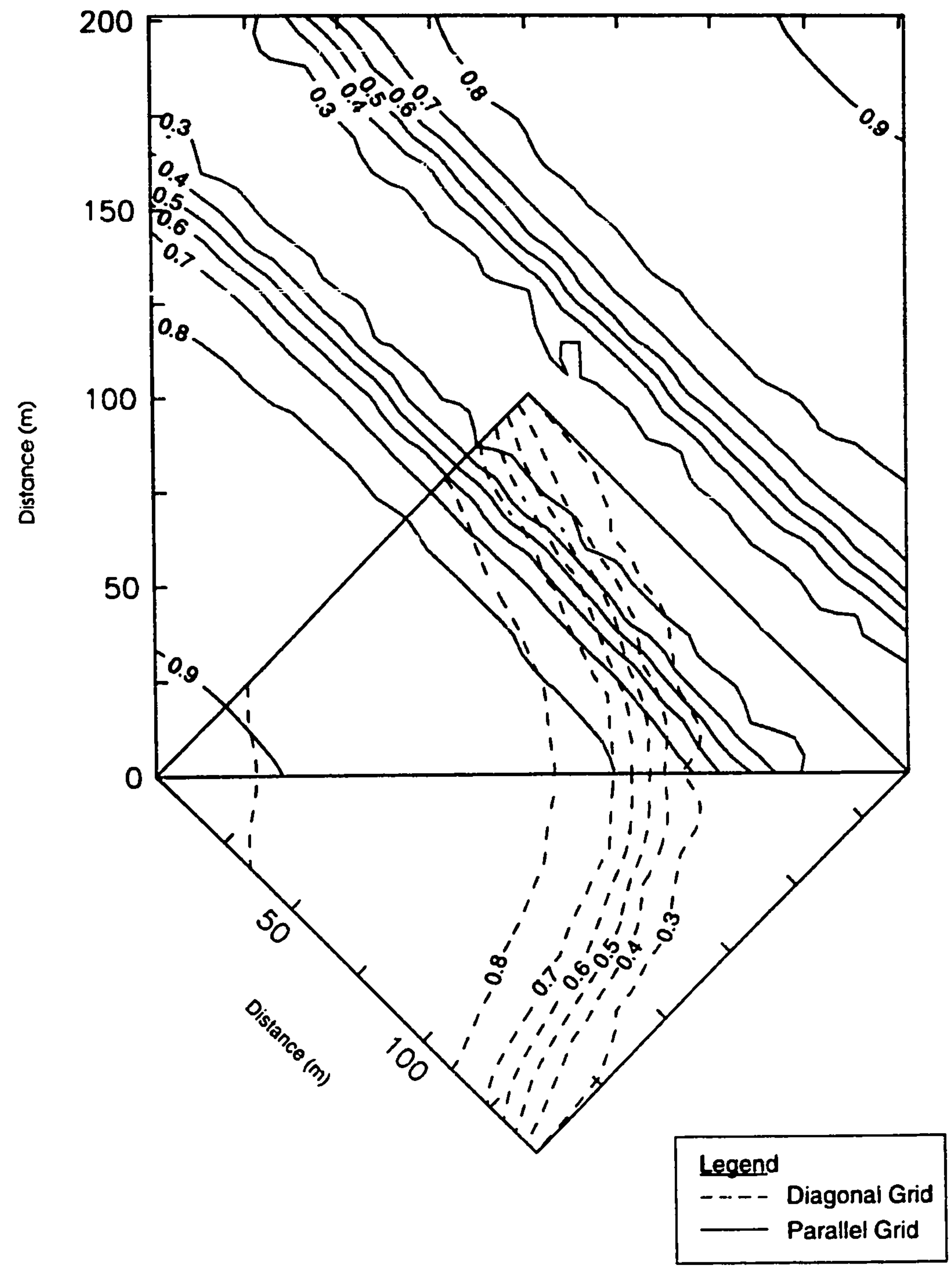

Fig. 10. Water saturation distributions obtained for the 5-spot water-flood problem using the 5-point finite-difference lattice option.

Hydraulic parameters include $k = 10^{-12}$ m^2, $\phi = 0.3$, $S_n = 0.1$, $S_{nr} = 0.1$ and zero capillarity, and relative permeability functions of Faust (1985) (see Table 6), with three-phase extension using the Stone-II function. To demonstrate the characteristic behavior of LNAPL and DNAPL, two otherwise identical simulations were performed with $\rho_n = 950$ kg m^{-3} and $\rho_n = 1200$ kg m^{-3}, which represent light and heavy oils, respectively.

The domain was discretized using a uniform grid consisting of 1936 (11 × 11 × 16) nodes and 1500 brick elements, and the simulation was performed for 2 yr. Shown in Fig. 15a is the developing light-oil lens for the LNAPL simulation. The plumes from the two sources move down to the water table and then move along the water-table surface to the downgradient boundary. Shown in Fig. 15b is the downward migration and pooling of heavy oil on the aquifer bottom for the DNAPL simulation. The plumes from the two sources migrate straight down through the water table to

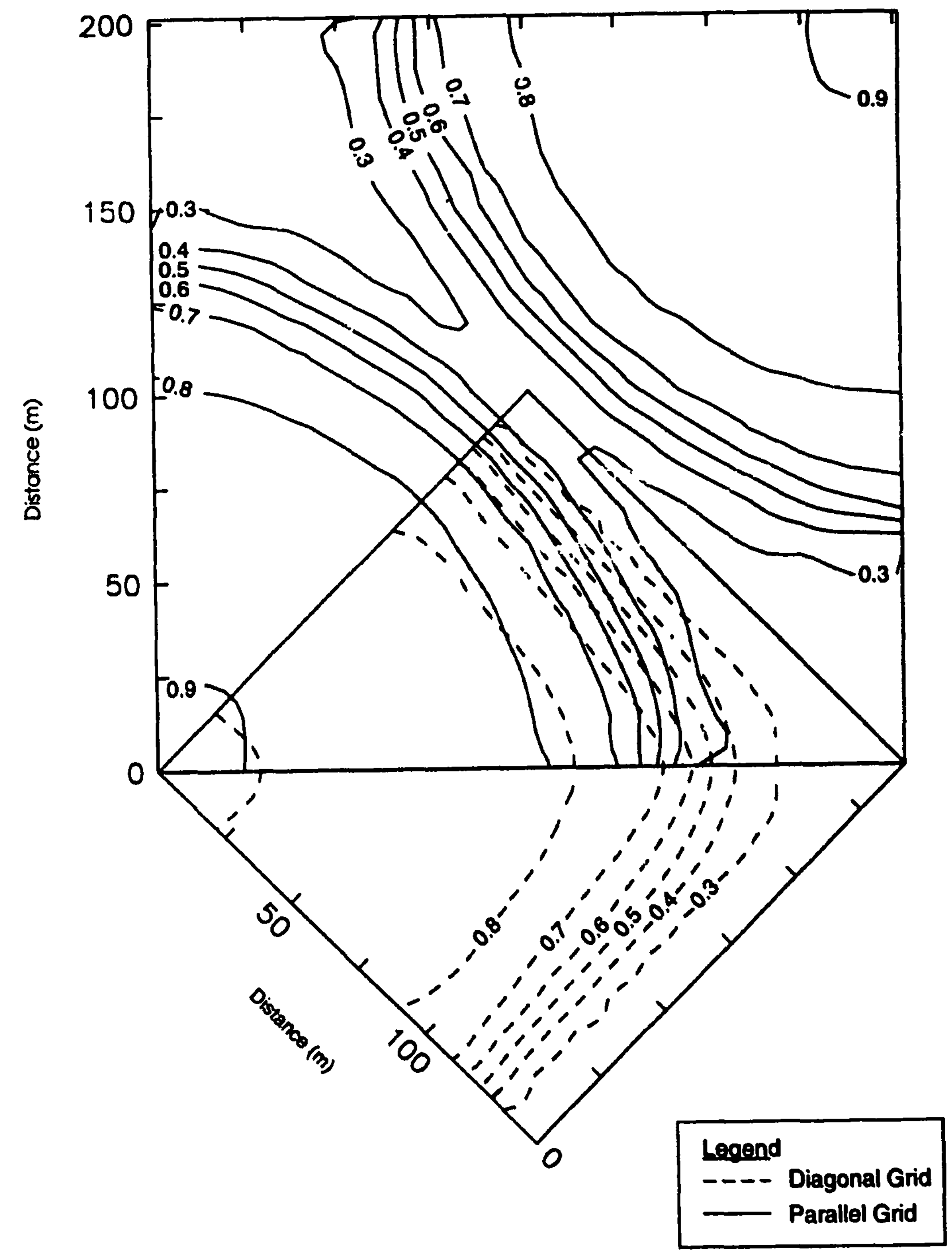

Fig. 11. Water saturation distributions obtained for the 5-spot water-flood problem using the 9-point finite-element lattice option.

the impervious bottom boundary. The NAPL from source *2* is almost at residual saturation by the time it mounds at the aquifer base. The NAPL from source *1* (the continuous release source) migrates down to the base where it mounds and moves downgradient with the ambient flow. The DNAPL is unaffected by the ambient flow till it reaches the impervious bottom boundary, because vertical gradients due to gravity effects are on the order of unity below the water table, while horizontal gradients due to the ambient flow are on the order of 0.01, with the assumed zero capillarity. Mounding of DNAPL at the aquifer base causes the lateral spreading of the plume while mounding coupled with ambient flow cause downgradient migration. The LNAPL simulation took $\sim$ 45 min to run on a 33-MHz *486*PC, with a total of 131 non-linear iterations for a simulation time of 565 days. The DNAPL simulation took $\sim$ 3 h on the same machine, with a total of 428 non-linear iterations for a simulation time of 490 days.

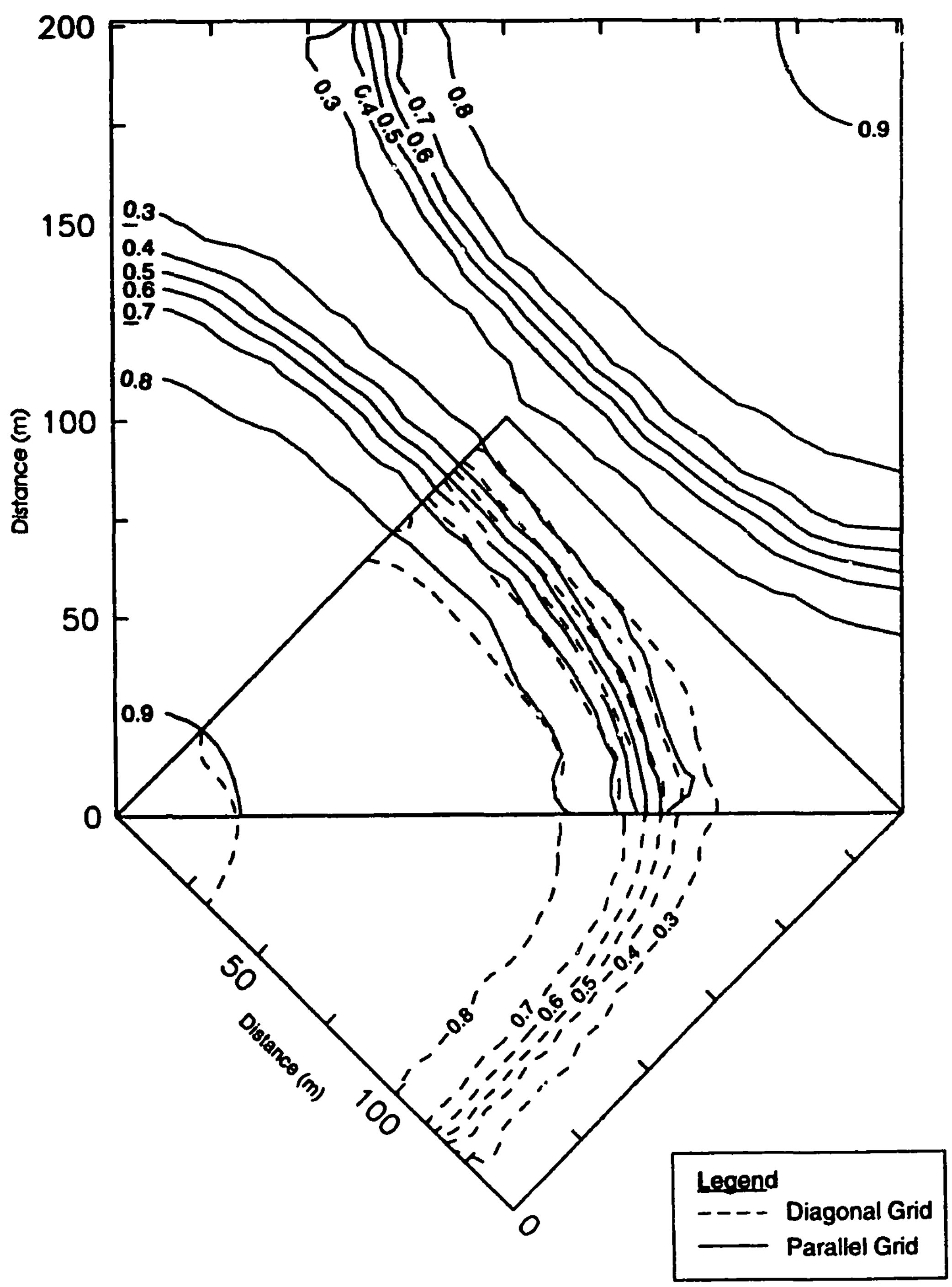

Fig. 12. Water saturation distributions obtained the 5-spot water-flood problem using the 9-point finite-element lattice option and a 2:1 grid aspect ratio.

6. Air-sparging simulation study

This problem was selected to study the flow dynamics of an air-sparging process. Relevant field site information given by Marley et al. (1992) is used for this study. The site of concern has been contaminated by gasoline from several leaking underground storage tanks in both the vadose and saturated zones. The average depth to the water table is $\sim$ 2.4 m below land surface. The contamination covers an area of $\sim$ 450 m^2. A preliminary assessment of the sparging influence radius and air velocities in the vicinity of an injection well may be obtained by considering variably saturated air flow only (i.e. assuming passive liquid phases). This modeling option, available in the code, was first used. A rectangular domain of 30 m $\times$ 20 m $\times$ 3 m was considered and discretized into 900 brick elements with 1232 nodes having uniform nodal spacings of $\Delta x = 2$ m, $\Delta y = 2$ m and $\Delta z = 0.5$ m. The initial conditions correspond to the water-

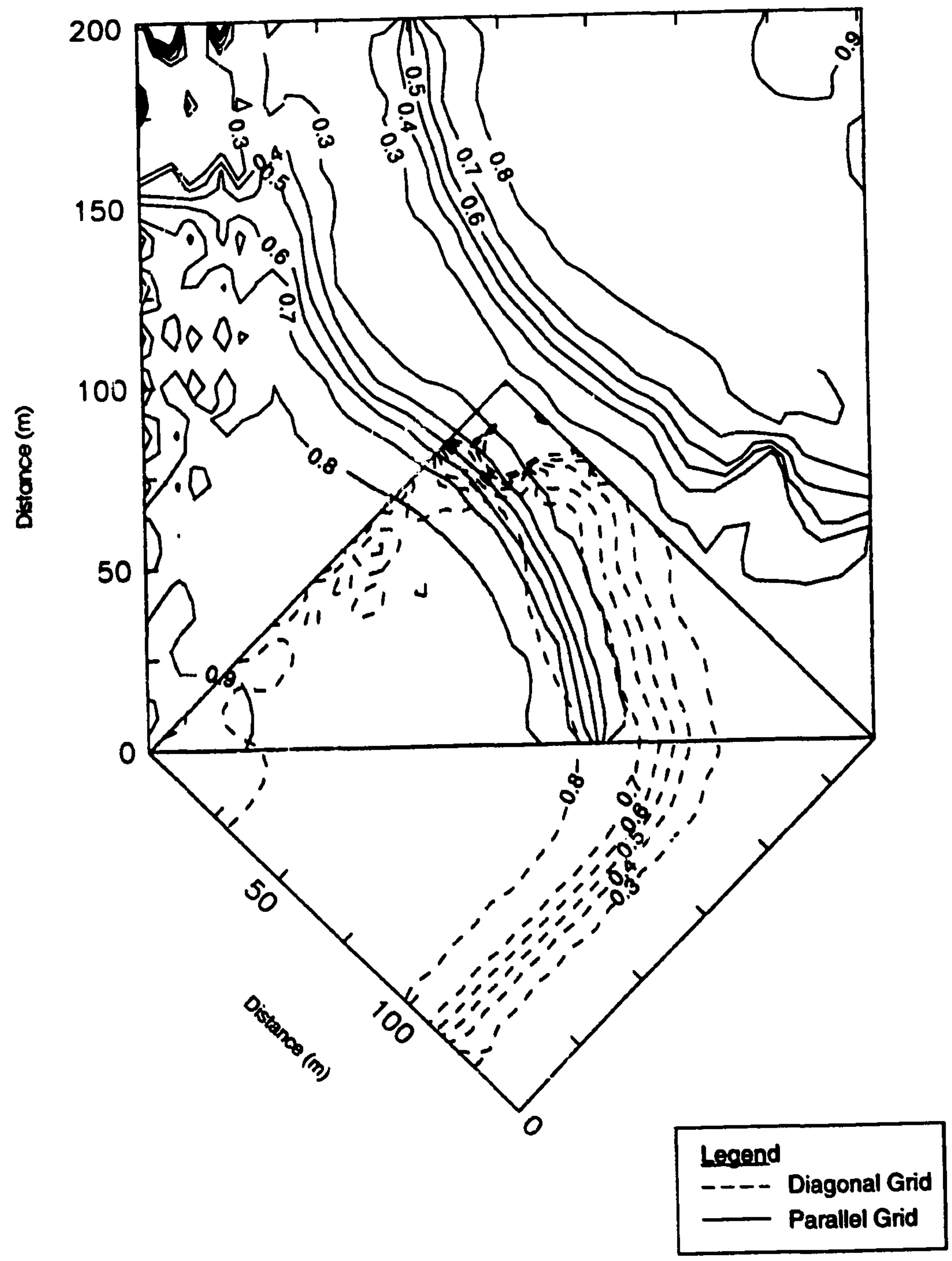

Fig. 13. Water saturation distributions obtained for the 5-spot problem using the conventional 9-point Galerkin finite-element scheme and a 2:1 grid aspect ratio.

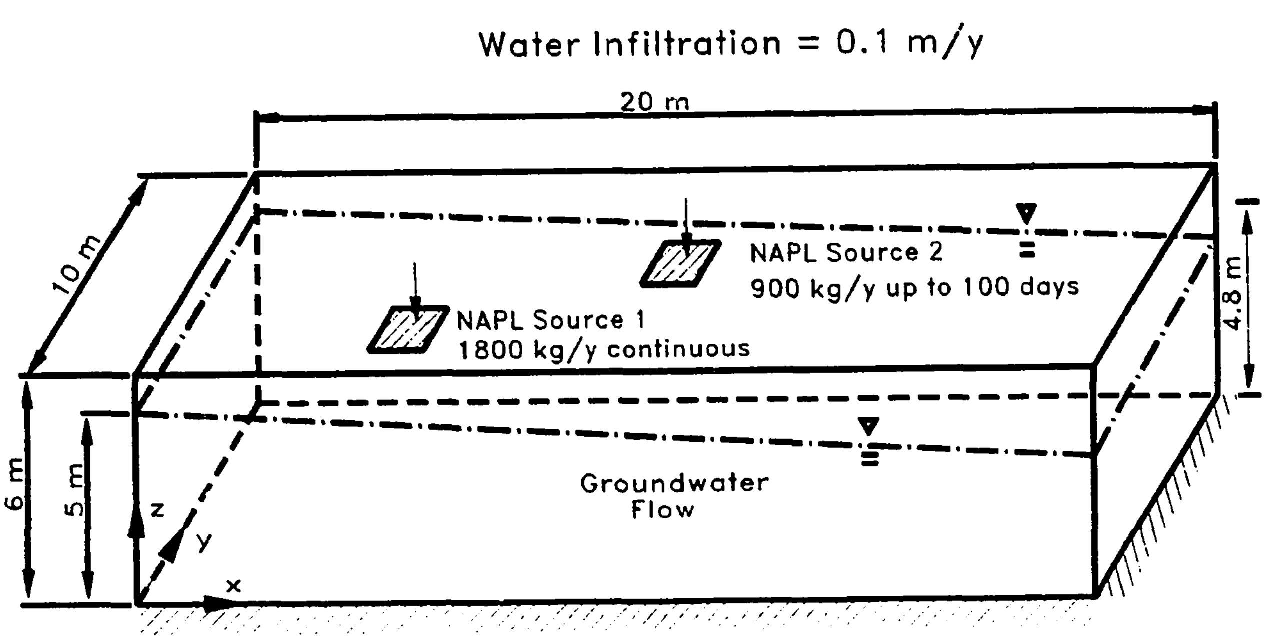

Fig. 14. Schematic description of 3-D problem of NAPL migration in a shallow aquifer.

table elevation 2.4 m below the top of the domain, and the prevailing atmospheric pressure in the vadose zone. The sparging process was created by injecting air at a steady rate of $1.773 \cdot 10^{-3}$ kg s^{-1} at the node located at $x = 10$ m, $y = 10$ m and $z = 1$ m (i.e. 0.4 m above the water table). Atmospheric pressure conditions were maintained on the surface boundary throughout the simulation and the bottom and lateral boundaries were treated as no-flow conditions. The soil and fluid properties used in the simulation (Table 8) were adopted from values given by Marley et al. (1992). The van Genuchten functions were used to describe the relative permeabilities and capillary pressure of the air–water system. The simulated steady-state distributions of air pressure in the vicinity of the well are depicted in Fig. 16, along with the available field data. The predicted and observed pressure profiles are in reasonable agreement. Note that for this base case, the model predicts a slight drop in air pressure with increasing elevation from 1 to 1.5 m. Although improved match with field values could have been obtained by calibrating the model, only site-specific values provided by Marley et al. (1992) were used. Due to the high degree of uncertainty in field information, the numerical results presented here should be viewed qualitatively. The air velocity patterns along a vertical cross-section and a horizontal plane passing through the well are shown in Figs. 17 and 18, respectively. Both figures depict the behavior of the air-sparging process.

For comparative purposes, a more rigorous analysis of the air-sparging problem was also performed using the two-phase formulation that considers both air and water as active fluid phases. The predicted air pressure and velocity fields are almost identical to those obtained from the passive-water-phase simulation.

An axi-symmetric analysis was also performed with the passive-liquid-phase assumption, for the same problem. The steady-state, air-phase pressure distribution along a horizontal line at $z = 1$ m and passing through the injection well location is shown in Fig. 19. The slight difference between the 3-D and axi-symmetric solutions in the vicinity of $x = 10$ m may be attributed to the boundary effects.

To gain further insight into the flow behavior, a parameter sensitivity study was conducted. The results obtained from several sensitivity runs were compared with the base case as depicted in Fig. 20. In light of the fact that the moisture movement does not have significant impact on the air flow, all of these cases were analyzed in 3-D mode with the air phase considered as the only active phase. In the first sensitivity run, the van Genuchten moisture retention parameter was increased by an order of magnitude (from 0.145 to 1.45 m^{-1}) to represent a more sandy type soil, with significantly less water retention capacity. It is noted that for this soil type, the sparge is ineffective, having a low pressure buildup and a very limited radius of influence. In the second sensitivity run, it was assumed that the upward flow of air at the top surface was blocked within a square patch (12 m × 12 m) centered at the injection well. A slightly greater pressure buildup and wider radius of influence were noted at the elevation of injection. Apparently, the sparge air pressure and influence radius were maintained at higher elevations. The remaining two sensitivity runs considered an order of magnitude reduction in the vertical permeability, and in both vertical and horizontal permeabilities, respectively. Both cases show greater pressure buildup (Fig. 20). It should be noted that lowering only vertical permeability (k_z) has a much

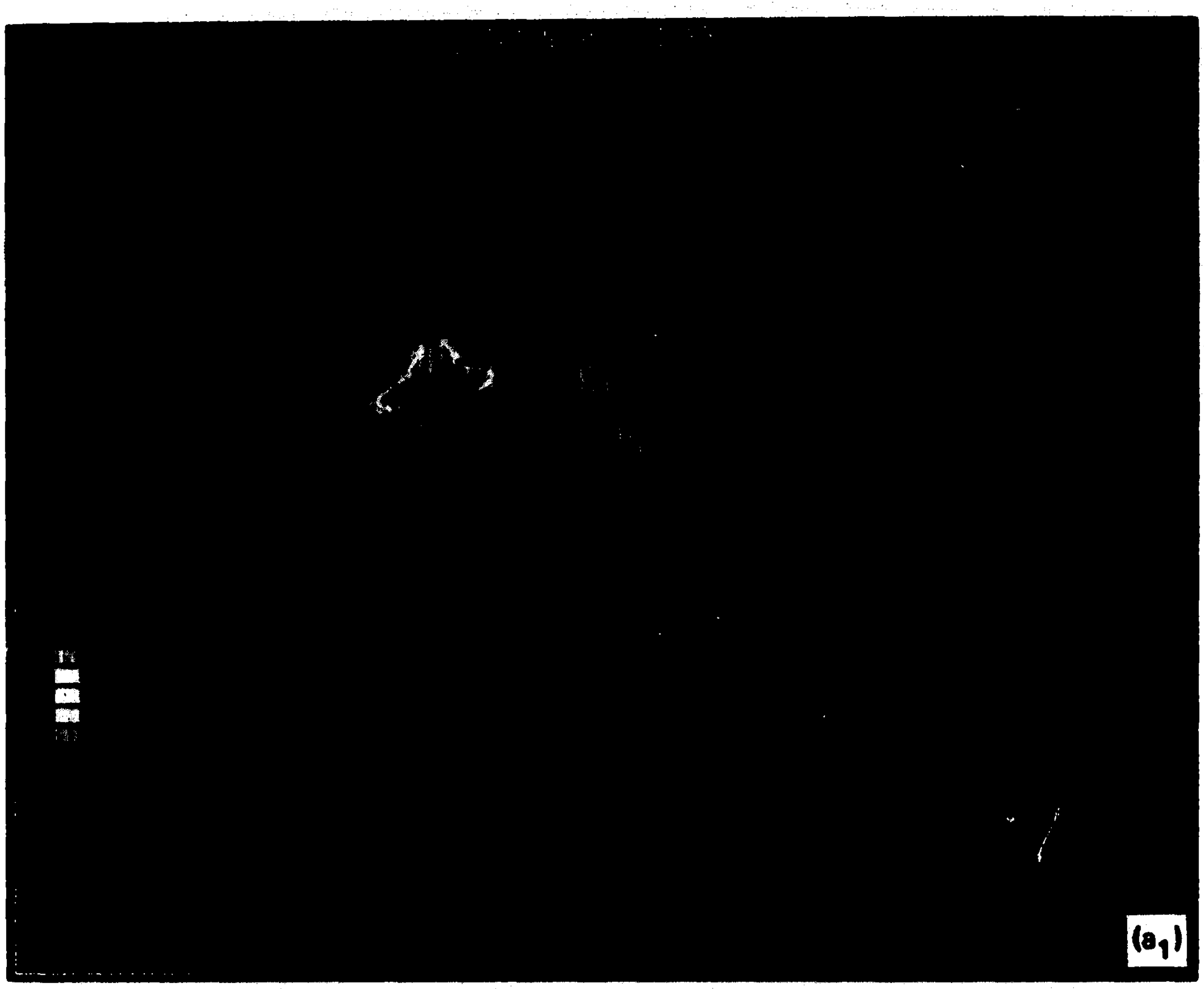

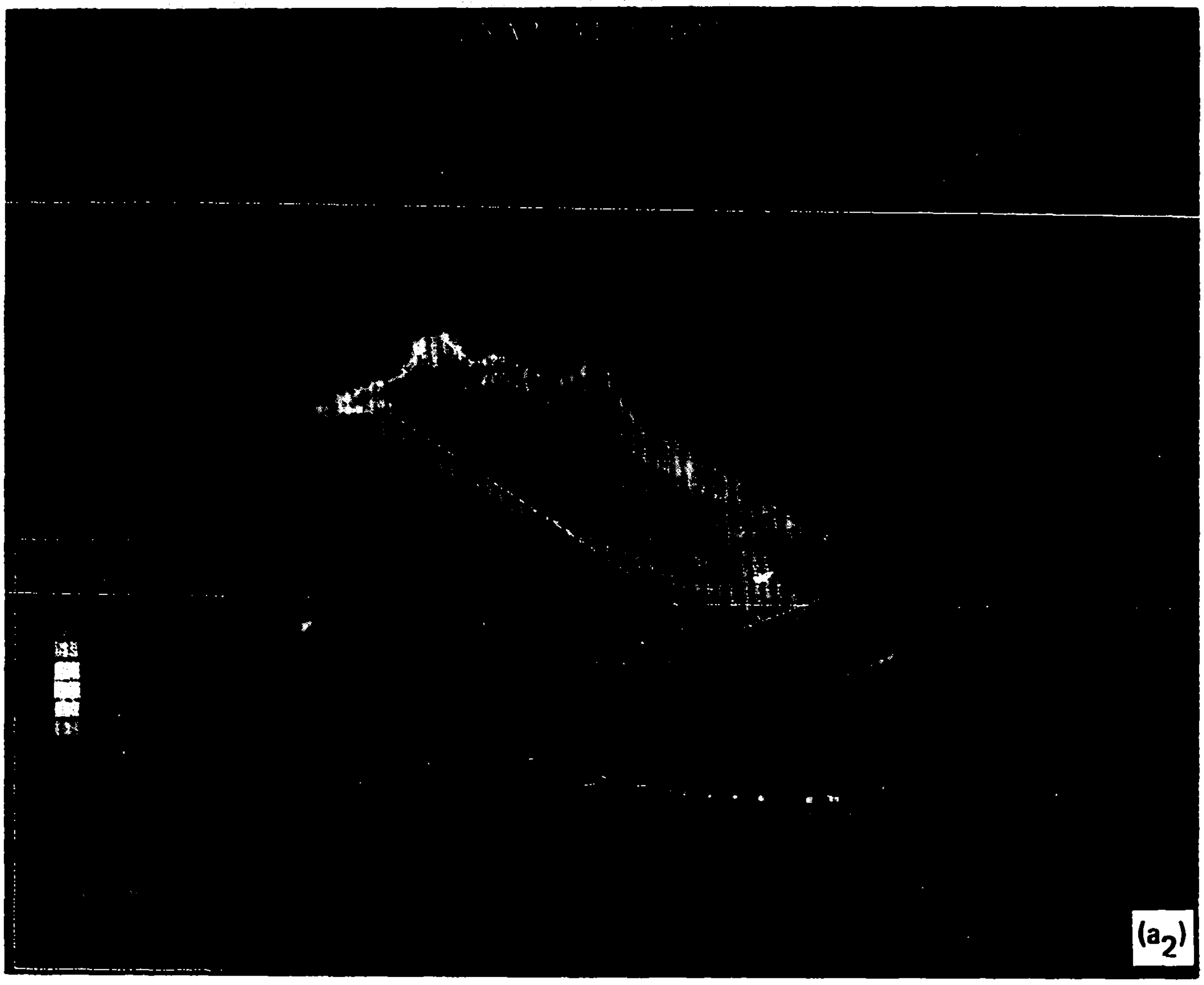

Fig. 15a. Simulated 3-D LNAPL plume at various time values.

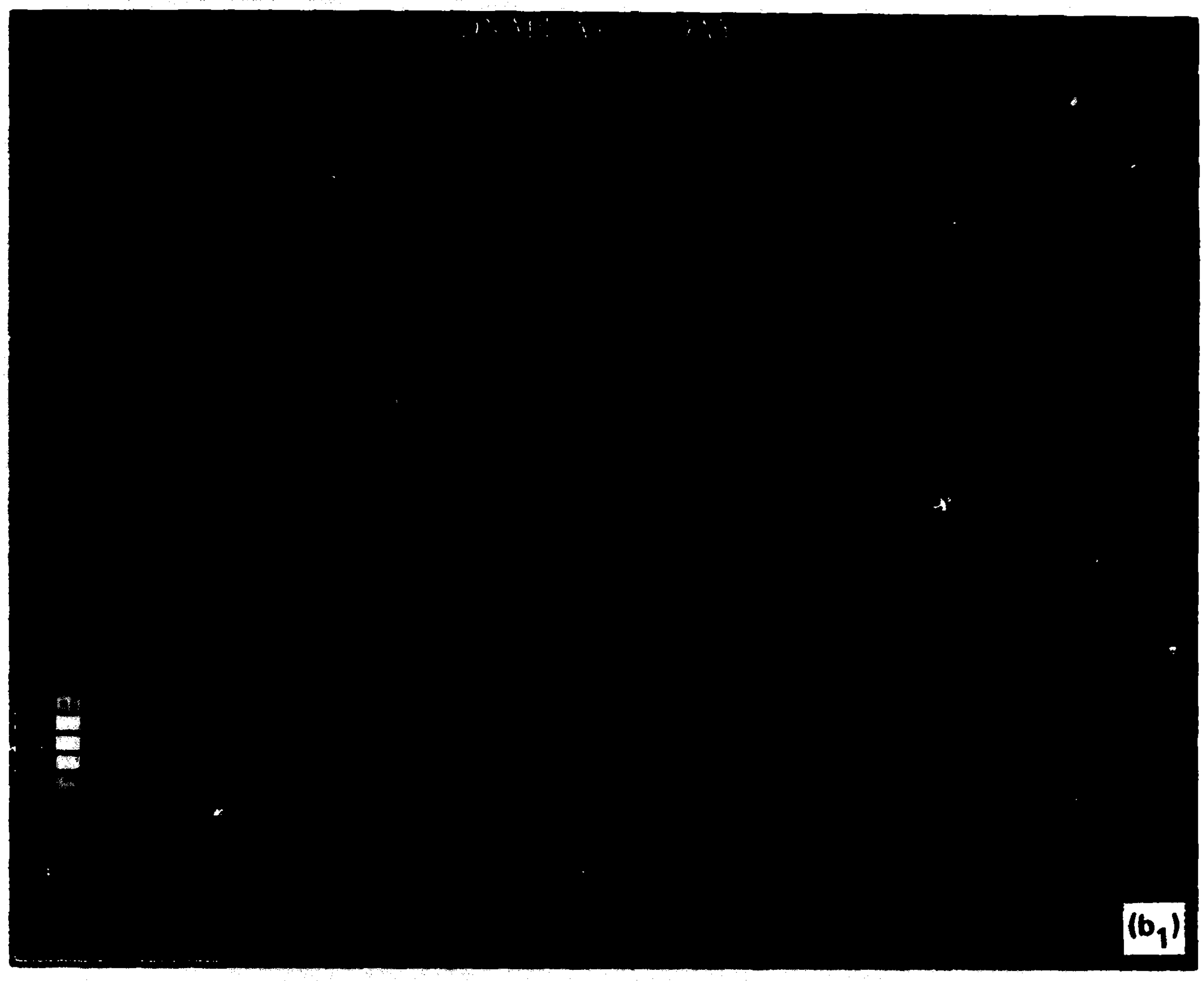

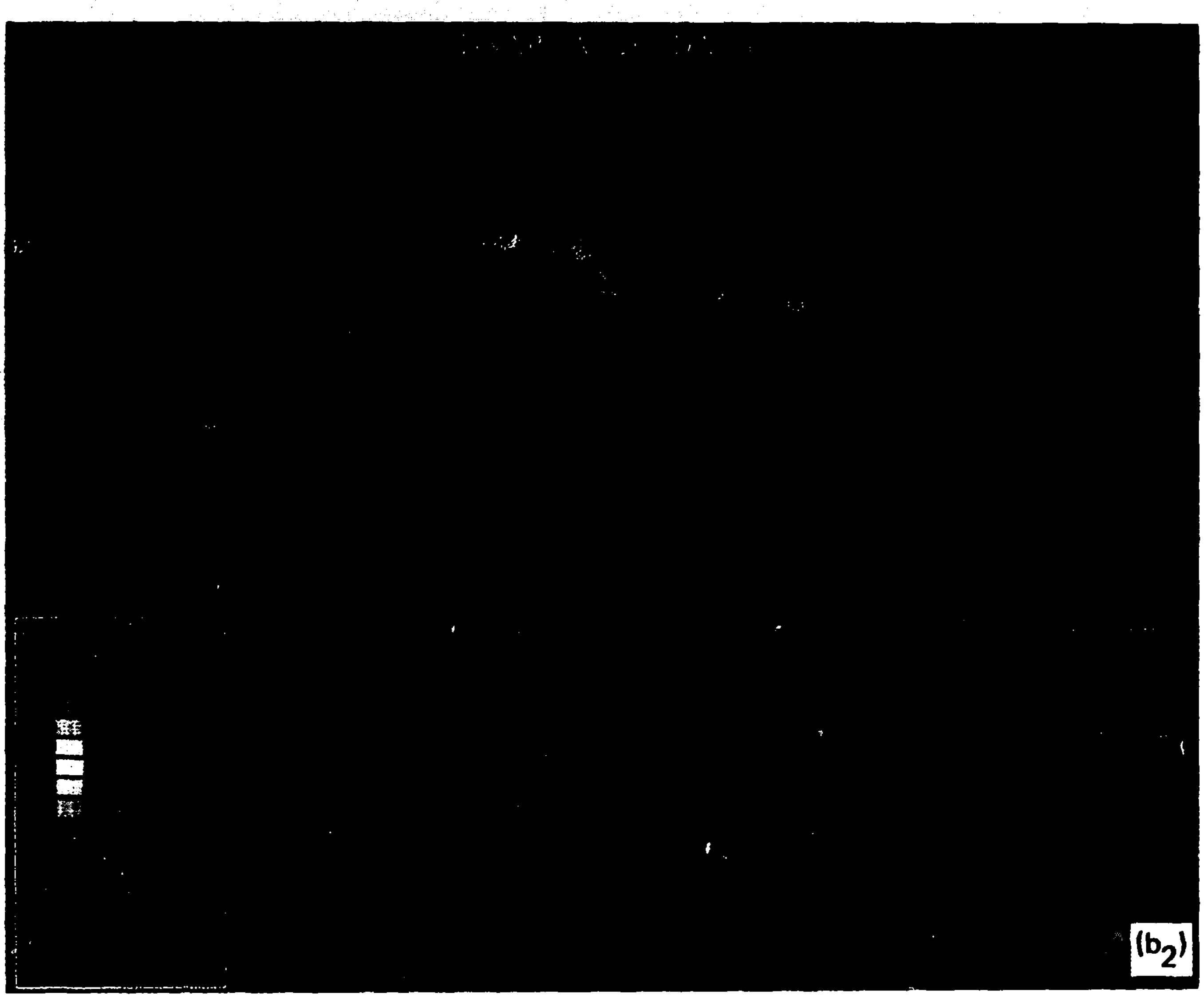

Fig. 15b. Simulated 3-D DNAPL plume at various time values.

Table 8
Material data for the air-sparging problem

Parameter	Value
Air injection rate, Q_a	$1.777 \cdot 10^{-3}$ kg s^{-1} (3.2 ft^3 min^{-1})
Intrinsic permeability, k	$2 \cdot 10^{-12}$ m^2
Porosity, ϕ	0.35
Water density, ρ_w	1,000 kg m^{-3}
Water viscosity, μ_w	0.5 cP
Air density, ρ_a	1.777 kg m^{-3}
Air viscosity, μ_a	$0.1983 \cdot 10^{-4}$ cP
Air compressibility, β_a	$1.7774 \cdot 10^{-5}$ Pa^{-1}
Residual water saturation, S_{wr}	0.40512
van Genuchten parameter, m	0.145 m^{-1}
van Genuchten parameter, n	2.7

greater impact on the sparge influence radius. Reducing only the vertical permeability leads to a significant increase in the sparge influence radius. Reducing horizontal and vertical permeabilities increases the sparge pressure applied at the well but does not affect the sparge influence radius significantly.

The results of the above sensitivity study thus indicate that sparging operations, in general, are more effective in water-retentive soils, with a large sparge radius of influence for layered or bedded soils. Furthermore, the sparge radius of influence diminishes with height, unless no-flow conditions are imposed at the surface.

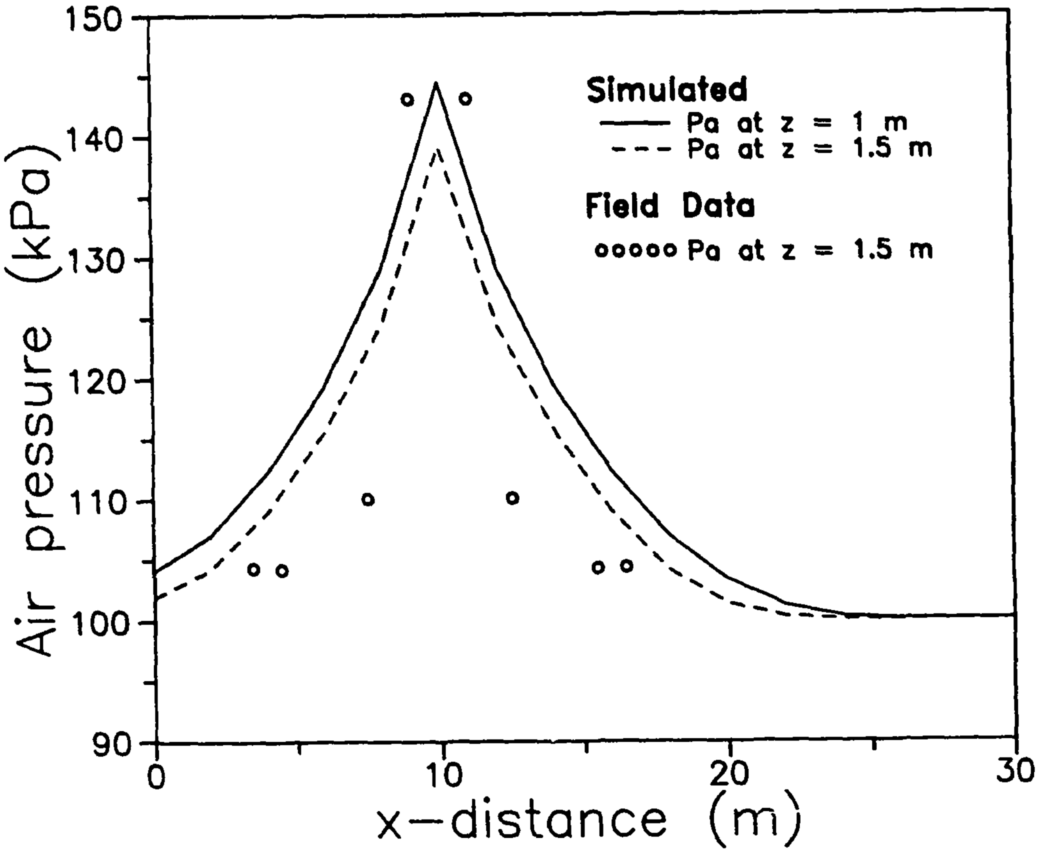

Fig. 16. Air pressure distributions for the air-sparging study (base case).

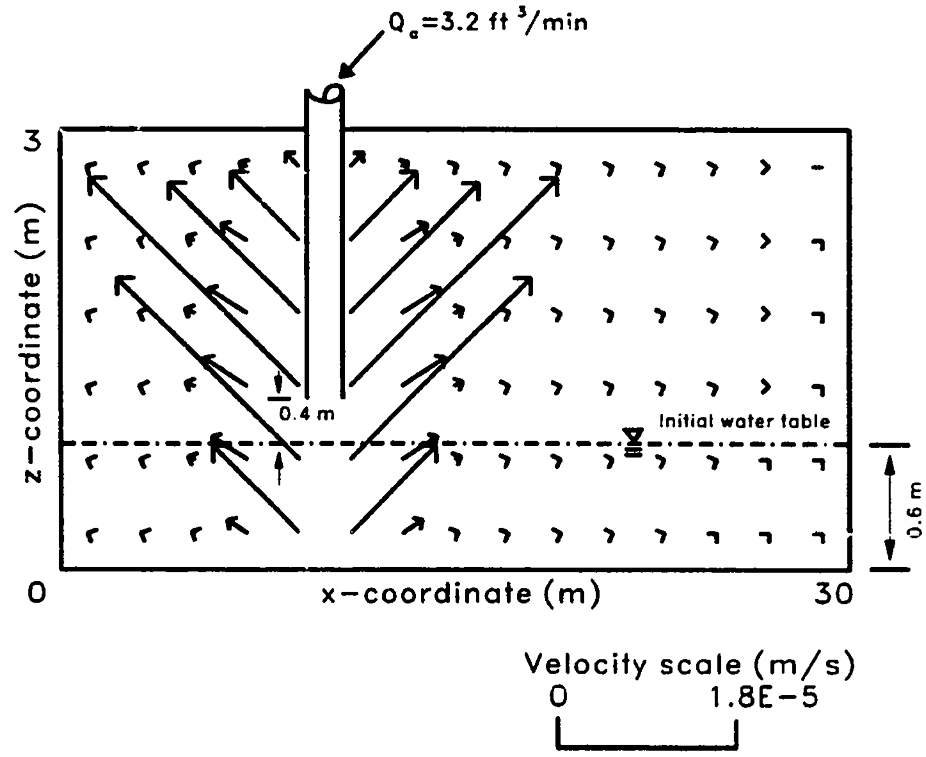

Fig. 17. Air-phase velocity vector plot through a cross-section passing through the sparging well.

7. Conclusions

The multiphase flow formulations discussed in Part 1 (Huyakorn et al., 1994 in this issue) have been implemented and tested using typical benchmark problems and field examples, and the various applicable simplifications to certain problems have been examined. The first simulation example shows some differences in results obtained from the fully three-phase and the passive-air-phase formulations, and verifies the performances of both formulations. For the one-dimensional (1-D) case studied, the surface boundary conditions for the air phase can have a considerable impact on the

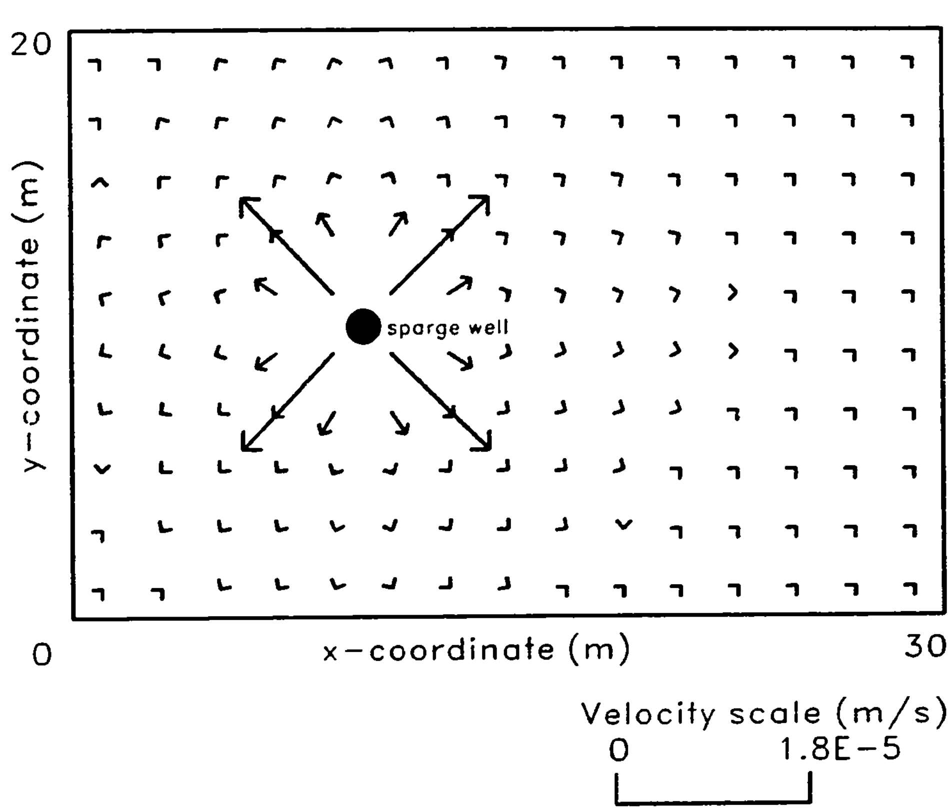

Fig. 18. Air-phase velocity vector plot through an areal plane passing through the sparging well.

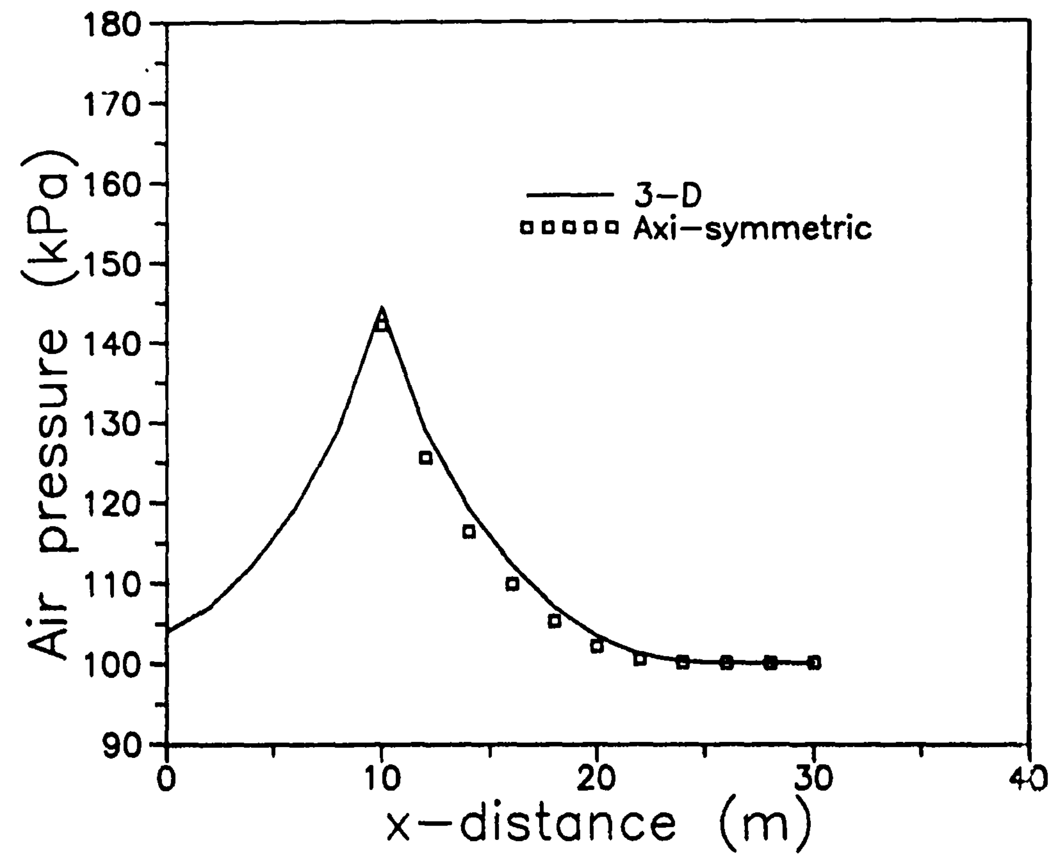

Fig. 19. Comparison of results from 3-D and axi-symmetric analyses (base case).

solution of the fully three-phase formulation, in the vicinity of the boundary. The second example examines the migration behavior of LNAPL and DNAPL with a 2-D cross-sectional analysis. The characteristic behavior of LNAPL is to spread laterally in the capillary fringe above the water table, while DNAPL migrates vertically down through the water table. The third example examines the 5-spot water-flood problem for an adverse oil–water mobility ratio. The 5-point, finite-difference and 9-point,

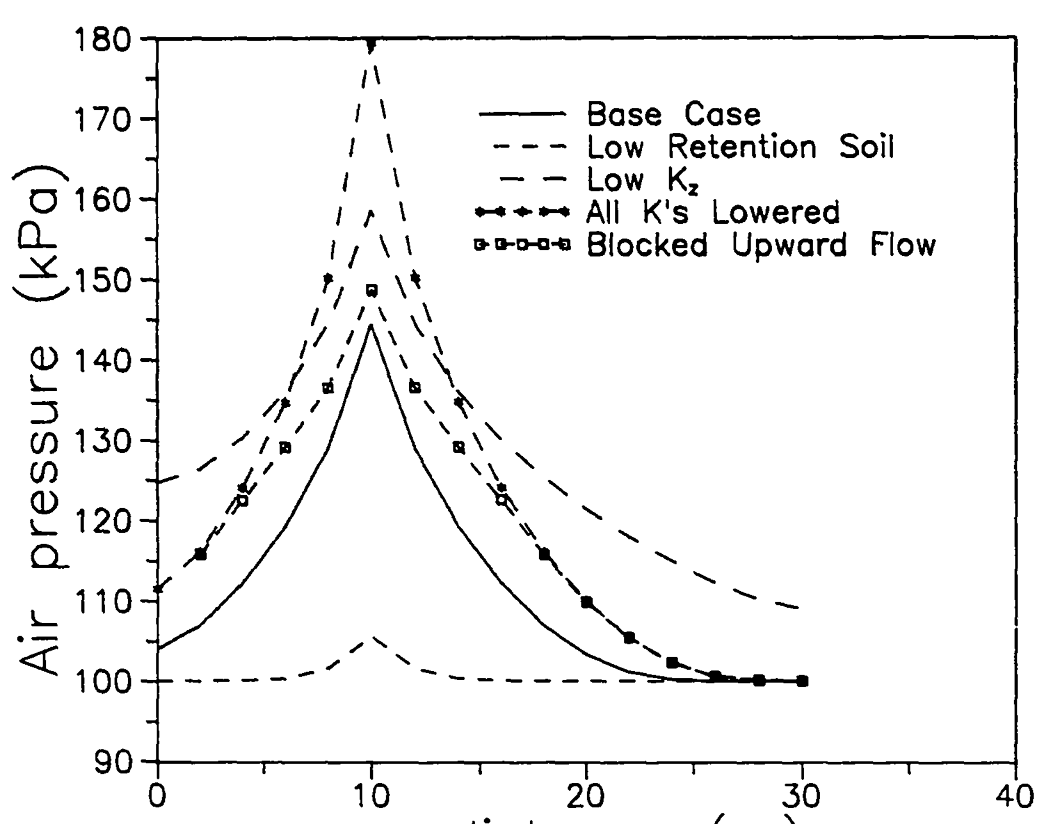

Fig. 20. Results of sensitivity analysis.

finite-element lattice options were tested with diagonal and parallel grids. The 9-point stencil performed well for both grids, while the 5-point stencil gave larger deviations in results between parallel and diagonal grids. The fourth example depicts the 3-D migration of DNAPL and LNAPL through an unconfined aquifer. The LNAPL migrates with the ambient groundwater flow, along the water table while the DNAPL sinks to the bottom, where it mounds and is then migrated downstream. The final example problem demonstrates the use of variably saturated air flow and two-phase flow formulations for an air-sparging study. The sparging process is further examined for various site conditions. Sparging is more effective in water-retentive soils, with larger values of sparge influence for stratified anisotropic conditions ($k_x > k_z$).

Acknowledgements

We would wish to acknowledge Dr. Peter Forsyth for furnishing numerical results from his compositional model. Thanks are also due to Dr. John Haselow and Seth Lawlor for providing assistance with three-dimensional data visualization and graphical presentation. Partial funding was provided by U.S. Department of Energy, Office of Technology Department

References

Coats, K.H. and Modine, A.D., 1983. A consistent method for calculating transmissivities in nine-point difference equations. Proc. Soc. Petrol. Eng. Symp. on Reservoir Simulation, San Francisco, CA, Nov. 15–18, 1983, SPE12248, pp. 155–173.

Faust, C.R., 1985. Transport of immiscible fluids within and below the unsaturated zone: A numerical model. Water Resour. Res., 21(4): 587–596.

Forsyth, P.A., 1988. Simulation of nonaqueous phase groundwater contamination. Adv. Water Resour., 11: 74–83.

Forsyth, P.A., 1990. A finite volume approach to NAPL groundwater contamination. University of Waterloo, Waterloo, Ont., Res. Rep. CS-89-46.

Forsyth, P.A., 1991. A control volume finite element approach to NAPL groundwater contamination. SIAM (Soc. Ind. Appl. Math.) J. Sci. Stat. Comput., 12(5): 1029–1057.

Forsyth, P.A. and Shao, 1991. Numerical simulation of gas venting for NAPL site remediation. University of Waterloo, Waterloo, Ont., Res. Rep. CS-91-06.

Gaucher, D.H. and Lindley, D.C., 1960. Waterflood performance in a stratified, five-spot reservoir — A scaled model study. Trans. AIME (Am. Inst. Min. Metall. Eng.), 219: 208–215.

Huyakorn, P.S. and Pinder, G.F.., 1978. New finite element technique for the solution of two-phase flow through porous media. Adv. Water Res., 2: 285–298.

Huyakorn, P.S., Wu, Y.S., Panday, S., Park, N.S. and Kool, J.B., 1991. SAMFT1D — Single-phase and multiphase flow and transport in 1 dimension, Ver. 2.0. Documentation and User's Guide.

Huyakorn, P.S., Panday, S. and Wu, Y.S., 1994. A three-dimensional multiphase flow model for assessing NAPL contamination in porous and fractured media, 1. Formulation. J. Contam. Hydrol., 16: 109–130 (in this issue; in this paper referred to as Part 1).

Marley, M.C., Li, F. and Magee, S., 1992. The application of a 3-D model in the design of air sparging systems. Proc. Conf. on 1992 Petroleum Hydrocarbons and Organic Chemicals in Ground Water: Prevention, Detection and Restoration, Nov. 4–6, 1992, Houston, TX, pp. 337–392.

Parker, J.C., Kaluarachchi, J.J., Kremesec, V.J. and Hockman, E.L., 1990. Modeling free product recovery at hydrocarbon spill sites. Proc. Conf. on Petroleum Hydrocarbons and Organic Chemicals in Ground Water, National Water Well Assoc..

Parker, J.C., Zhu, J. and White, H., 1992. Modeling phase separated hydrocarbon migration and recovery in anisotropic fractured media. Proc. Conf. on Petroleum Hydrocarbons and Organic Chemicals in Ground Water: Prevention, Detection, and Restoration, Houston, TX, Nov. 4-6, 1992, pp. 255-267.

Thomas, G.W., 1982. Principles of Hydrocarbon Reservoir Simulation. Int. Human Resour. Dev. Corp., Boston, MA, 207 pp.

Willhite, G.P., 1986. Waterflooding. Soc. Pet. Eng. Textbook, Vol. 3, 326 pp.

Yasonik, J.L. and McCracken, T.A., 1979. A nine-point finite-difference reservoir simulator for realistic prediction of unfavorable mobility ratio displacement. Soc. Pet. Eng. J., 19: 573-592.